University of Tennessee, Knoxville
TRACE: Tennessee Research and Creative Exchange

Doctoral Dissertations | Graduate School

12-2013

# Beta-Delayed Neutron Spectroscopy of Fission Fragments Using the Versatile Array of Neutron Detectors at Low Energy

Stanley Vincent Paulauskas
*University of Tennessee - Knoxville*, spaulaus@utk.edu

Follow this and additional works at: https://trace.tennessee.edu/utk_graddiss

## Recommended Citation

Paulauskas, Stanley Vincent, "Beta-Delayed Neutron Spectroscopy of Fission Fragments Using the Versatile Array of Neutron Detectors at Low Energy. " PhD diss., University of Tennessee, 2013.
https://trace.tennessee.edu/utk_graddiss/2606

This Dissertation is brought to you for free and open access by the Graduate School at TRACE: Tennessee Research and Creative Exchange. It has been accepted for inclusion in Doctoral Dissertations by an authorized administrator of TRACE: Tennessee Research and Creative Exchange. For more information, please contact trace@utk.edu.

To the Graduate Council:

I am submitting herewith a dissertation written by Stanley Vincent Paulauskas entitled "Beta-Delayed Neutron Spectroscopy of Fission Fragments Using the Versatile Array of Neutron Detectors at Low Energy." I have examined the final electronic copy of this dissertation for form and content and recommend that it be accepted in partial fulfillment of the requirements for the degree of Doctor of Philosophy, with a major in Physics.

Robert K. Grzywacz, Major Professor

We have read this dissertation and recommend its acceptance:

Witold Nazarewicz, Carrol Bingham, Lawrence H. Heilbronn

Accepted for the Council:

Carolyn R. Hodges

Vice Provost and Dean of the Graduate School

(Original signatures are on file with official student records.)

# Beta-Delayed Neutron Spectroscopy of Fission Fragments Using the Versatile Array of Neutron Detectors at Low Energy

A Dissertation Presented for the
Doctor of Philosophy
Degree
The University of Tennessee, Knoxville

Stanley Vincent Paulauskas
December 2013

© by Stanley Vincent Paulauskas, 2013
All Rights Reserved.

*For my Father and Grandmother, one taught me how to work the other taught me how to cahoot.*

# Acknowledgments

I express my deepest thanks to all of the fantastic and thoughtful teachers, professors, and mentors through the years. I would like to thank Mr. John Paquet for his guidance and for providing me the tools necessary to solve any problem. Without his passion for teaching physics and more importantly life, I would never have discovered such a rich and fulfilling field of study. My deepest gratitude goes to the late Dr. David Murdock who provided more guidance on homework problems than the probably should have but always embodied the most important qualities of a stellar mentor.

I would like thank Dr. Miguel Madurga-Flores for many insightful and sometimes explosive conversations about the research presented in this thesis. A special thanks goes to Dr. David Miller for helping me to finally understand C++, answering a plethora of tedious programming questions, and, most importantly, sharing a passion of fiery foods. Dr. Michael Bertolli deserves many thanks for his help understanding statistics and the finer points of fitting data. Our many conversations have provided the stimulating distractions necessary to finish my studies.

I would be remiss not to acknowledge my thesis advisor Dr. Robert Grzywacz for throwing me off the deep end and providing enough guidance to keep me from drowning. Finally, I must thank my family for their continued support during my studies and life, and Ms. Jessica Hamilton for somehow putting up with the rigors of my entire graduate life.

*I am disillusioned enough to know that no man's opinion on any subject is worth a damn unless backed up with enough genuine information to make him really know what he's talking about.*

H. P. Lovecraft

# Abstract

This work details the study of nuclear decay in the region of doubly magic 78Ni using the Versatile Array of Neutron Detectors at Low Energy (VANDLE). This detector system uses the time-of-flight technique to measure the energy of beta-delayed neutrons. VANDLE uses a fully digital data acquisition system equipped with timing algorithms developed as part of the experimental work. The experiment examined nearly 30 beta-delayed neutron precursors produced at the Hollifield Radioactive Ion Beam Facility at Oak Ridge National Laboratory. This work discusses three of these nuclei: 77,78Cu and 84Ga. Results from the experiment provide details of the Gamow-Teller decay in neutron rich nuclei near 78Ni.

# Table of Contents

# List of Tables

# List of Figures

# Chapter 1

# Background and Motivation

## 1.1 Introduction

Beta decay is the most common mode of nuclear decay, see Figure 1.1. This nuclear transformation, mediated by the weak interaction, has decay lifetimes that can be much longer than decays associated with other interactions. For example, the electromagnetic force mediates gamma ray emission from an excited nuclear state and typically occurs on the order of picoseconds. In the simplest picture, beta decay is the transformation of a proton(neutron) into a neutron(proton) along with the emission of an positron(electron) and neutrino(anti-neutrino). This process does not change the atomic number of the nucleus.

Beta decays may be broken into two distinct classes: allowed and forbidden. Allowed transitions, also called Gamow-Teller (GT) transitions [3], are the most common form of decay. The total angular momentum and isospin of the parent and daughter nuclei can change by $\pm 1$ or 0 units. The orbital angular momentum and parity of the nucleus remains unchanged. In contrast, forbidden transitions [4, 5] involve the leptons carrying angular momentum away from the nucleus generally yielding a smaller decay probability. The most common form of forbidden decay is the first forbidden (FF) transition, which involve changes in orbital angular momentum

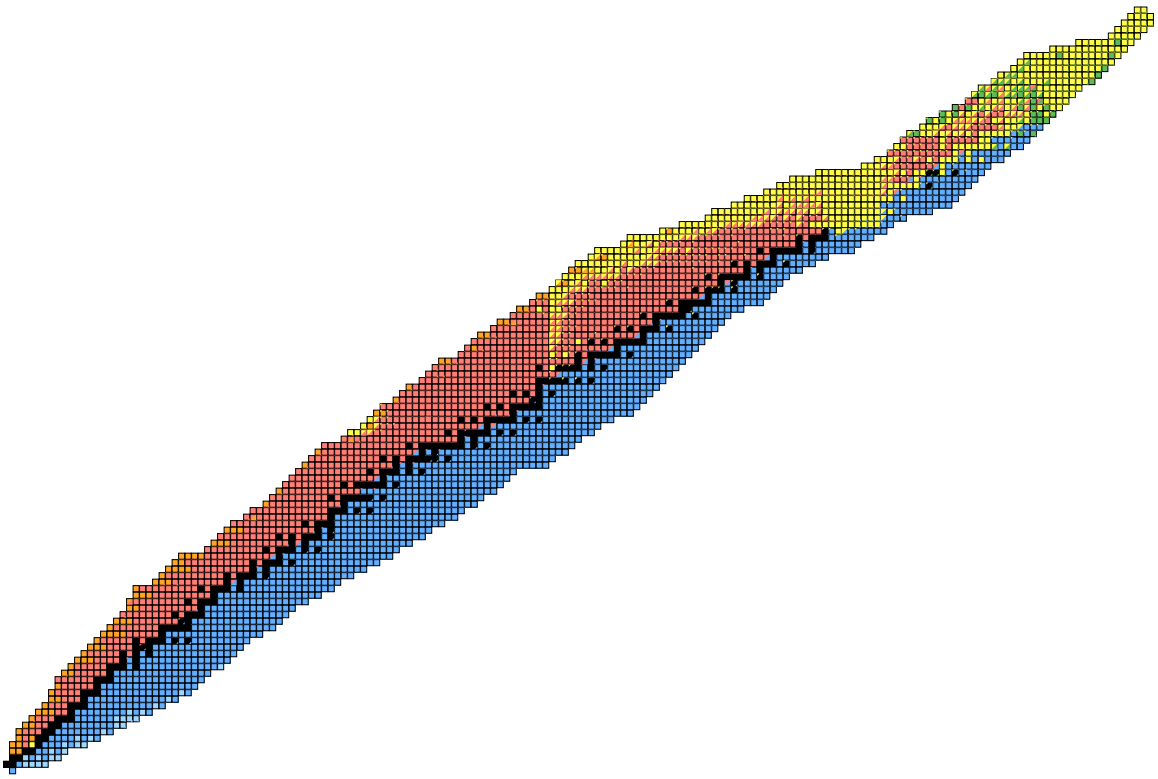

Figure 1.1: The chart of nuclides plotting proton number (Z) versus neutron number (N). Black squares represent stable nuclei, light blue squares represent $\beta^-$ decay, red squares $\beta^+$ decay, yellow represent $\alpha$ decay, and green represent fission.

and parity change. The total angular momentum can change by 0, 1, or 2 units. The parity change occurs when the emitted electron and neutrino couple to an odd value of angular momentum with respect to the nucleus [6].

One can write the lifetime of a nuclear state in the following form:

$$T_{1/2}^{-1} = \sum_{E_i \geq 0}^{E_i \leq Q_\beta} S_\beta(E_i) \times f(Z, Q_\beta - E_i). \tag{1.1}$$

The parameter $Q_\beta$ refers to the energy difference between the ground state (g.s.) of the parent and daughter nuclei, $E_i$ is the energy of the final state in the daughter, and Z is the number of protons in the decay daughter. The $f(Z, Q_\beta - E_i)$ term 1.1 is the Fermi integral. The Fermi integral is related to the kinematic phase space and can be derived from the relativistic Dirac equation. Its strong dependence on $Q_\beta$ tends to shorten nuclear lifetimes as $Q_\beta$ increases and quenches decays to highly excited final states. The second term in Eqn. 1.1, $S_\beta(E)$ is the beta decay strength function. This contains the reduced transition probabilities for the decay, which are the matrix elements for the GT operator[7].

## 1.2 Theoretical Models

We can begin to describe the matrix elements and beta decay through the nuclear shell model. The nuclear shell model, similar to the atomic shell model, describes the protons and neutrons in the nucleus as belonging to distinct oscillator shells provided by a harmonic oscillator basis plus a residual interaction between nucleons. For example the GT transitions discussed above may be viewed as the transformation of spin-orbit partners in single particle orbitals (shells). A critical development in the shell model was the idea of spin-orbit coupling [8, 9]. The spin-orbit coupling assumes that orbitals with higher angular momenta have higher binding energy, and

this effect explains the origins of the "magic" numbers seen in atomic nuclei. Spin-orbit coupling also gives rise to the crossing of orbitals, which, as we shall see, is an important feature in GT transitions.

Solving the shell model can quickly become intractable if one considers all of the nucleons in the calculation. However, magic numbers provide a natural choice for framing the calculation into a core and valence space. The core consists of a nucleus with only paired nucleons (e.g. $^{78}$Ni) and is separated from the valence space by a large shell gap. The valence space is then any nucleons outside of this core, and the Hamiltonian used to calculate the matrix elements is replaced by an effective one [10]. This reduces the problem to one of diagonalization within the valence space. A commonly used method, the Lanczos method [11], is advantageous that the complexity increases linearly with the size of the matrix to be diagonalized, making it computationally fast and efficient.

While the shell model description is useful and describes the behavior of nuclei well, it is not the only model that one may choose. Some approach the problem from the idea of mean-fields and the quasi-particle random phase approximation (QRPA), which uses the Hartree-Fock-Bogoliubov method to calculate basis states [12, 13]. Others use the QRPA with the finite range droplet model (FRDM) [14], which derives its basis from modeling the equation of state of the nucleus. Both models represent microscopic models as they take into account the specific interactions between the nucleons. Takahashi and Yamada proposed another approach to the problem in the the gross theory of $\beta$ decay [15], which proposes the $S_\beta$ in the form of the Gamow Teller Giant Resonance. The model calculates information about the average properties of the nuclei, but contains no information about the single particle structure.

## 1.3 The $^{78}$Ni Region

Of interest to this work is the region of neutron-rich nuclei surrounding $^{78}$Ni. This region of the nuclear landscape is interesting for many reasons. From the perspective

of fundamental nuclear physics, this region holds interest due to the fact that the nuclear shell structure may change as nuclei become more neutron rich. This is illustrated by the change in the ground state spin-parity in odd-A Cu isotopes [16, 17] and by the hypothesized emergence of sub-shell gaps (N = 58) as one crosses the N = 50 shell closure [18].

The astrophysical rapid neutron capture process (r-process) originates in this region [19] and detailed knowledge of nuclear data is extraordinarily valuable. The r-process occurs in supernovae and is thought to be one of the major sources of elements heavier than iron and for nuclei at closed shells the neutron capture cross section drops. These are called waiting point nuclei and the process must "wait" for beta decay until the neutron capture resumes [19]. The abundance of some elements sharply increases due to the presence waiting points. Many astrophysics calculations must rely on extrapolations of known data into the exotic regions; however, as previously mentioned the behavior of exotic nuclei may be different than less exotic species. Accurate models of the r-process require the neutron capture cross sections and beta decay half lives to be experimentally determined [20, 21].

Lastly, the nuclei in this region are abundantly produced in the fission of $^{235}$U and their properties influence the operation of nuclear reactors [22]. The design stages of a reactor must take into account the amount and energy distribution of neutrons emitted from the fission fragments. The modeling of transportation and storage of spent fuel require experimentally determined inputs. This means that there must be careful study of the beta decay half-lives and neutron cross sections for fission products. These data are necessary for inputs into the decay heat calculations. The decay half-lives will also have an effect on the reactor cooling time. This information is necessary for environmental and safety considerations.

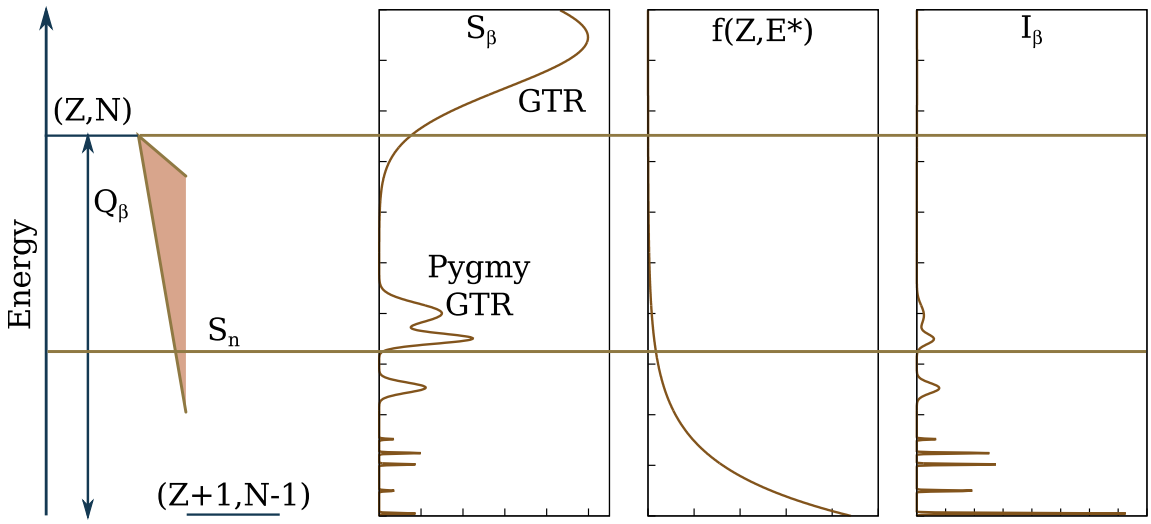


Figure 1.2: A schematic of the energetics of the beta decay. $S_\beta$ is the $\beta$ strength distribution, f(Z,E*) is the Fermi function, and $I_\beta$ is the measured intensity spectrum.

## 1.4 Decay of Exotic Nuclei

Close to the line of nuclear stability, the energetics of the beta decay are such that the daughter nucleus is left in a neutron bound state. Deexcitation proceeds via the emission of characteristic gamma rays. This does not hold true as one moves into more exotic nuclei. Because the Q-value becomes larger, the excitation energy ($E^*$) of the daughter may be greater than the neutron separation energy ($S_n$) allowing for the possibility of neutron emission. This process, discovered by Edwin McMillan and others in 1939 [23], plays a significant role as a tool for nuclear structure diagnostics and discovery. Schematically one may view this process as shown in Figure 1.2. In the $^{78}$Ni region, the branching ratio of the decay can be understood through the competition between GT decays and FF decays. When N>50 (Fig. 1.3), it is difficult to generate an allowed GT transition to states with low excitations in the daughter nucleus. This is due to the large neutron excess and the Pauli exclusion principle. The GT transitions will only be able to connect neutron states occupying negative parity $fp$ orbitals that are below the N=50 shell gap with negative parity $fp$ proton states above the Z=28 closure. The GT transformation of the valence $g_{9/2}$ neutrons

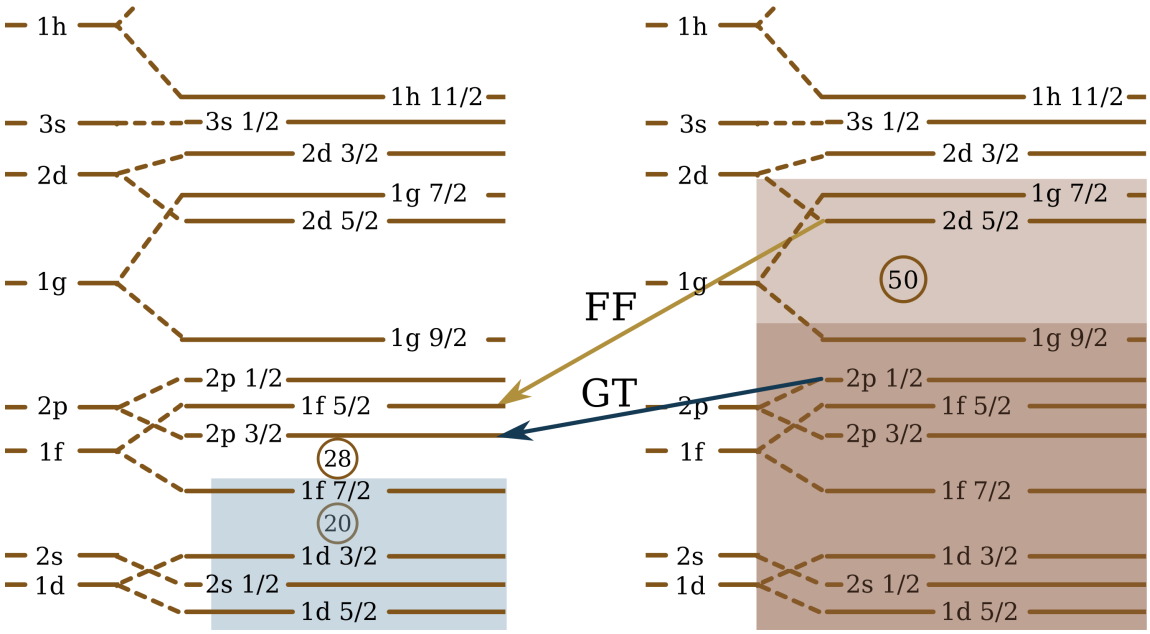


Figure 1.3: The a schematic model of the shell structure near $^{78}$Ni showing the two different decay paths, FF and GT. The shaded blue region corresponds to the filled proton shells. The dark brown square represents the shells of interest when N < 50 and the light brown corresponds to after one crosses the N = 50 shell gap.

is difficult because the spin-orbit partner $g_{7/2}$ lies above Z=50 shell gap. A transition between the $g_{9/2}$ neutrons into the proton $g_{9/2}$ state is also available. However, in this case a GT decay will create a deeply bound neutron hole that leaves the nucleus in a highly excited state. Population of highly excited states will favor beta delayed neutron emission. For decay with large $Q_\beta$ windows, the forbidden transitions may be able to provide an alternate decay path to states with lower excitation energy.

The competition between GT and first forbidden transitions manifests itself in the gamma emission spectrum by producing two distinct groups of gamma lines [24, 25]. This competition leads to erosion of the beta delayed neutron emission. Borzov [26] recently studied the interplay of allowed and forbidden decays on beta delayed neutron emission. His calculations show the step-like behavior of beta delayed-neutron emission at the N=50 crossing due to the Q value increase for pure GT transitions

and the effect of forbidden transitions on the branching ratios, see Figures 3 and 4 in Ref. [26].

## 1.5 Previous Work on Beta-Delayed Neutrons from Fission Fragments

Both theoretical and experimental work provide a rich history study of beta-delayed neutron emission from fission fragments. This field of study saw great interest from about 1970 until the middle of the 1990s. This is due to the development of detector systems capable of high energy resolution, and isotope separation techniques. The fission of $^{235}$U produces the isotopes to be studied, and $^{3}$He and $CH_4$ ionization chambers measured neutron energies. Discrete lines in the neutron energy spectrum indicated the presence of the distinct states in the daughter nucleus emitting neutrons [27, 28]. These spectra allowed extraction of information about the nuclear structure and how it influences the process of beta decay.

Perhaps the most controversial work in the field is the idea of the Pandemonium effect [29, 30]. Pandemonium is a fictional nucleus meant to demonstrate that the structure seen in particle emission spectra (gamma or neutron) is due to statistical fluctuations. Statistical effects alone govern the decay of the pandemonium nucleus, and the observed structures in the spectra have no connection to nuclear structure. The neutron emission spectra for this nucleus behaves similarly to those studied by Kratz et al.[28]. While the spectra do not agree with complete accuracy, the overall gross structure and behavior of the spectra agree quite well. This leads Hardy et al. to state that one should exercise caution when interpreting beta-delayed neutron spectra and that any interpretation of these data must consider pandemonium.

More recent theoretical work on the subject uses a combination of QRPA and the Hauser-Feschbach statistical model [31, 32]. QRPA calculates the $\beta$-decay probabilities of states in the daughter nucleus. These states decay either via gammas

or neutrons, and the Hauser-Feschbach model calculates the branching ratios. This method explicitly takes into account spin and parity selection rules and generally predicts the correct energy range of neutrons in the decay. However, the model does not reproduce the discrete peaks seen in the experimental spectrum. This theoretical framework bears consideration because it takes into account both of the major goals of these types of studies: the nuclear structure effects and the statistical effects.

Interest in the study of beta-delayed neutron emission waned in the mid 1990s for several reasons. First, technical challenges in radioactive ion beam production meant that the production of these exotic nuclei would be difficult or impossible with the required purities and rates. Second, the detector systems lacked the efficiency required to measure exotic nuclei. Finally, pandemonium played a large role in the interpretation of the experimental spectra and the analysis may not be interesting for nuclear structure.

## 1.6 Current Work

This work brings about a revival of the interest in beta-delayed neutron spectroscopy of fission fragments. The primary focus of the work addresses the challenges mentioned above. The Holifield Radioactive Ion Beam Facility (HRIBF) provided high purity and high rate beams of the exotic nuclei of interest. To take advantage of these exotic beams, the Versatile Array of Neutron Detectors at Low Energy (VANDLE), see Figure 1.4, was constructed and provides high neutron detection efficiency. It measures neutron energies via the time-of-flight technique. A key development in VANDLE is the use of a digital data acquisition system, which provides the high neutron detection efficiency. Newly developed timing algorithms provide the necessary time resolutions for measuring the neutron's time of flight.

This work is the first to apply the time-of-flight technique to fission fragments and used VANDLE to measure nearly 30 known beta-delayed neutron emitters, and obtained the neutron energy spectra, many measured for the first time. High purity

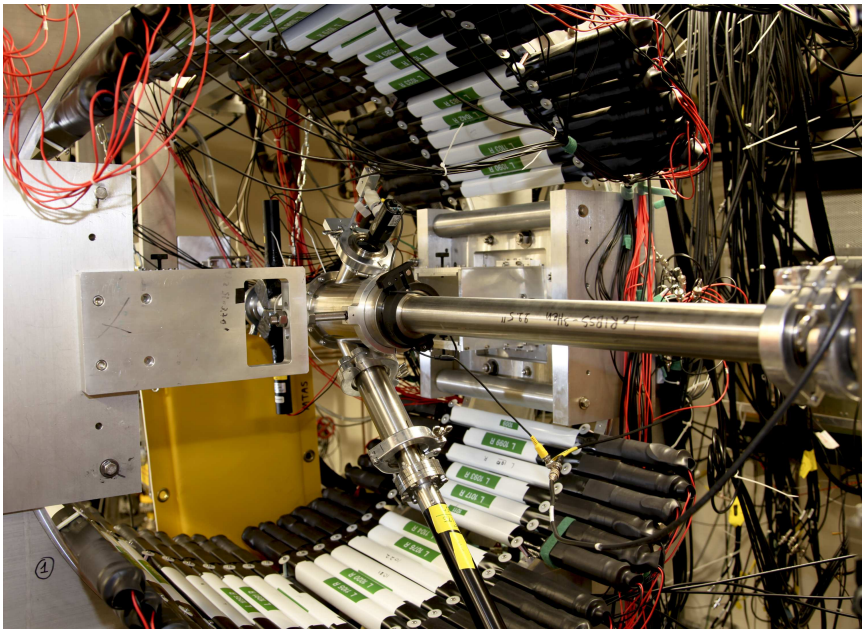

Figure 1.4: A picture of the VANDLE setup at the HRIBF.

gamma ray detectors enable coincidence measurements to be made between gamma rays and neutrons, which, it will be shown, is essential to understanding the structure and behavior of the delayed neutrons. Some prominent cases are presented, $^{77,78}$Cu and $^{84}$Ga. These nuclei exhibit clear evidence for strong "resonance" structures in the neutron energy spectra, with the strongest in $^{84}$Ga. Because of the strong quenching of the decays to high energy states by the Fermi function and the high density of states in this region of excitation energies, this result is surprising. The peak structure must be due to strong GT transition matrix elements.

# Chapter 2

# Digital Data Acquisition Systems

## 2.1 Introduction

In this work, we present critical development steps for the Versatile Array of Neutron Detectors at Low Energy (VANDLE) [33, 34]. These steps include the implementation and characterization of timing algorithms and a new triggering model. These developments enable VANDLE to be fully instrumented with a digital data acquisition system. Digital data acquisition systems are rapidly becoming common in nuclear physics experiments due to their many advantages with respect to analog electronics [35, 36]. The main feature of such systems is a reliance on numerical algorithms that operate on digitized representations of the electrical pulse from a detector. The flexibility offered by an unlimited choice of pulse shape analysis methods is one reason for the growing demand of these systems.

However, an important limitation of this approach is the finite amplitude and time resolution of the analog to digital converters (ADCs) used to digitize the signals from the detectors. As a result, the digital image of the signal is a distorted version of the "real" signal. This distortion comes from the the frequency cutoffs imposed by the implementation of an analog filter [37], which is a common component of digital systems. The finite bit and sampling resolution is particularly important for the "fast"

signals from scintillator detectors. In order to be recorded with high fidelity, signals from these detectors require subnanosecond sampling frequencies. This enables the digital algorithms to extract information about the signal for the highest relevant frequencies. The availability of gigahertz (GHz) digitizers makes it possible to store signals with subnanosecond accuracy. Unfortunately, these systems suffer from high energy consumption and carry an expensive price-per-channel burden.

Digital timing algorithms extract the time of arrival of a signal from the digitized waveform. Ideally, the timing resolution should only be limited by the detector performance not by the digitizer. This problem can be solved for fast signals using gigahertz digitizers and a digital constant fraction discrimination (DCFD) algorithm [38]. This solution is often difficult or impractical if one is instrumenting a large detector array. As an alternative one could employ slower digitizers (e.g. 100 MS/s) but the timing resolution for these systems may not be adequate for the timing needs.

In experimental nuclear physics, many time-of-flight neutron detectors consist of plastic scintillators, which have signal rise/decay times on the order of a few nanoseconds [39, 40, 41, 42]. These detectors rely on analog electronics with conventional CFDs to obtain precise timing. In contrast, nuclear technology applications, e.g. positron emission tomography, use gigasamples-per-second (GS/s) digitizers with fast scintillators, e.g. lutetium orthosilicate (LSO), for timing applications. The time information is extracted using a DCFD or a model is fit to the digitized waveform [43]. These GHz systems are capable of obtaining resolutions on the order of hundreds of picoseconds. Using a 40 MS/s digitizer with LSO, Streun et al. perform a linear fit between two points on the leading edge of the waveform to obtain resolutions of 2 ns [44]. These studies demonstrate the necessity of using different algorithms depending on the digitization frequency of the system.

Past work involving digital timing techniques by a University of Florence group applied a 100 MS/s digitizer to signals from a silicon detector [45]. These tests used a digital constant fraction discriminator to achieve timing resolutions on the order of

hundreds of picoseconds. Their work demonstrates the necessity for the proper choice of algorithms to determine timing less than the sampling frequency of the digitizers.

To instrument VANDLE, a choice between traditional NIM and digital electronics needed to be made. Digital electronics provided an ideal solution due to previous experience within the group, and their low cost per channel. Ideally, one would instrument VANDLE with GS/s digitizers to minimize the development time necessary to achieve sub-nanosecond time resolution. VANDLE requires many channels of instrumentation and GHz digitizers are still prohibitively expensive. Therefore, we investigated the capabilities of lower frequency systems for the timing applications. This work used XIAs DGF Pixie-16 100 and 250 MS/s digitizers to process the signals from VANDLE.

The challenge is to demonstrate that precise time information can be extracted from the digitized signal when the sampling period is much longer than the characteristic time scale of the signal. While many algorithms exist to accomplish this task, they are not necessarily applicable to every timing situation. The algorithm must take into account the response of the digital system to the raw signal. A Nyquist filter [37] and the sampling frequency of the ADC govern the response. Thus, the problem of timing becomes a deconvolution problem where the major challenge is to determine relevant folding (response) function.

This work tested three numerical algorithms to extract timing information from the digitized signals: a digital constant fraction discriminator (DCFD), a fitting algorithm (FA), and a weighted average algorithm (WAA). To verify these algorithms, a new method to verify the robustness of the digital timing algorithm was developed. The system was tested using an arbitrary waveform generator providing fixed shape pairs of waveforms with various amplitudes and delays. Finally, the digital timing was applied to signals from a plastic scintillator coupled to a photomultiplier tube (PMT). It will be shown that commercially available digital systems, with a low cost per channel, can be used for high resolution timing measurements with fast scintillators.

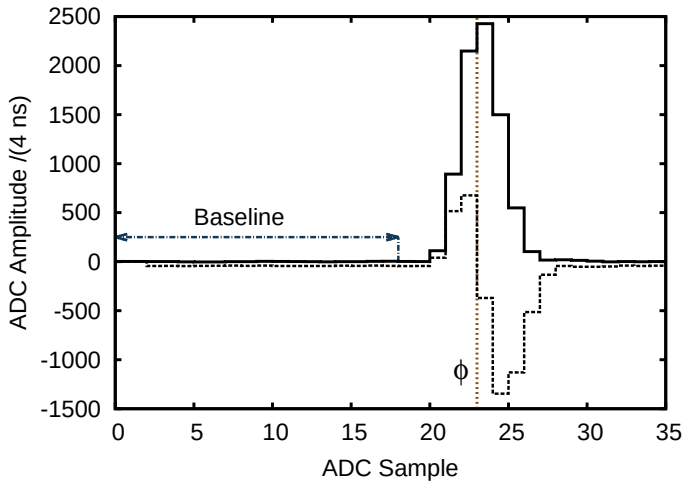


Figure 2.1: A sample trace from the 250 MS/s system using the signal produced by the AFG (solid line). The dashed line represents the DCFD for this trace. The position of $\phi$ is given by the vertical dashed line and is given by zero crossing of the DCFD calculated using Equation 1 with D = 1 and F = 0.75. The horizontal dashed arrow denotes the region used to determine the baseline.

## 2.2 Testing Setup and Software Analysis

This work used an 100 MHz Tektronix AFG3102C Arbitrary Function Generator (AFG) [46]. This function generator allows control of the delay between the signals with 10 ps resolution, their width with 10 ps resolution, and amplitudes with 0.1 mV resolution. A pulse of 10 ns width approximated signals from plastic scintillators. A time calibrator with variable rate triggered the AFG. One volt signals, using half of the ADCs dynamic range, provided a reference signal for the FA. The jitter in the arrival time of signals produced by the AFG is on the order of 50 ps as measured by a 2.5 GS/s oscilloscope. The outputs from the AFG were connected to two adjacent channels in the Pixie-16 digitizers.

The data is read out from the digitizer via a MXI-4 fiber optic crate controller and processed into a data file through a C++ software package. An in-house developed C++ analysis software suite unpacks the data files and processes the raw data stream. A configuration file maps the raw module and channel in the data stream to a specific

detector type and performs the appropriate processing. For the work presented here the software applies the timing algorithms to every digitized waveform in the data stream. The average amplitude of all bins up to the signal in the trace constitutes the baseline, denoted by the horizontal dashed arrow in Figure 2.1. The standard deviation of the baseline for the AFG is no larger than 1 ADC bin for the cases presented in this work. All of the discussed timing algorithms are implemented in this stage of the analysis and not on-board the digitizer.

## 2.3 Digital Timing Methods

For the Pixie-16 systems used in this work, the digital filter implemented in the FPGA latches and records the digitized waveforms (traces) once a valid trigger is detected. The total trace length and pre-trigger length can both be adjusted by the user. The arrival time of the recorded trace consists of two components. The first component is a 48-bit timestamp, which is the real-time counter value of the FPGA latched at the time of the valid trigger. The time resolution of such a timestamp is obviously limited by the processing clock frequency of the FPGA. The second component is derived from the trace, which is latched with respect to the first component. This position is referred to as the phase ($\phi$), and it will be shown that $\phi$ can be determined to a precision that is smaller than the sampling frequency of the digitizer. The time of a given event in the digitizer is provided by the summation of the filter clock from the FPGA and the phase.

The response of the digital system to a time translation of the raw signal that is below the sampling frequency depends on the derivative of the digitized trace [47]. If the derivative is not constant in the interpolation region, one cannot extract accurate time information using linear methods. If the digitization frequency is substantially faster than the input signal one may assume local linearity. Because the transit times of the scintillators used in this work are much shorter than the digitization period, one can rarely construct a situation where local linearity is achieved. Timing algorithms

that do not take into account the non-linear response of the system will not produce accurate results. For these reasons, this work investigated three timing algorithms.

First, the DCFD provides a simple algorithm and was demonstrated to work with digitizers [38, 45]. The DCFD applies the following equation to the digitized waveform:

$$DCFD[k] = Fy[k] - y[k - D]. \tag{2.1}$$

D is the delay, F is the fraction of the original trace and y[k] is the baseline subtracted amplitude of the trace at bin $k$ [38]. Figure 2.1 shows an example of the output of the DCFD algorithm, where D = 1 and F = 0.75, for the 250 MS/s system with the associated trace.

The obvious limitation of this algorithm is that the smallest delay available will be equal to the sampling period. To measure subsampling delays, we apply an Akima spline [48] to the data points. Akima splines have a smoother interpolation than a cubic spline, and will produce fewer unnatural spikes in the interpolation. The GNU Scientific Library (GSL) provided the splining algorithms [49]. The spline function increases the number of points available to determine the zero crossing in the hopes of making the behavior of the leading edge of the trace linear in that region. A linear interpolation between points above and below the zero crossing determines its position to better than a sampling cycle.

In a second method, an algorithm fit the digitized waveform. The analytic model approximates the response of the digital system. For this work the function took the following form:

$$f(t) = \alpha e^{-(t-\phi)/\beta}(1 - e^{-(t-\phi)^4/\gamma}). \tag{2.2}$$

The parameter $\beta$ is the decay constant for the exponential, which is related to the decay of the waveform. The leading edge of the waveform is described by the inverted-squared Gaussian, whose width is given by $\gamma$. The normalization of the signal is given

by $\alpha$. The offset $\phi$ provides the phase of the signal. An averaged waveform fit with all free parameters in Eqn. 2.2 optimizes $\beta$ and $\gamma$. These fitted values are held constant for the timing analysis.

For the pulser signals, the standard deviation of $\beta$ and $\gamma$ is 0.01 ns and 0.001 $ns^4$, respectively. For signals from the detectors described in Section 3.4, the standard deviation is 0.3 ns and 0.1 $ns^4$, respectively. Fitting 16000 traces where all FA parameters are free provides a sample of the possible $\beta$ and $\gamma$ values. The sample variance of the set assumes a normal distribution. The square root of sample variance provides the standard deviation of $\beta$ and $\gamma$.

The timing analysis is carried out using a non-linear least squares fitting routine provided by GSL, henceforth referred to as the fitting algorithm (FA). The fitter uses a Levenberg-Marquardt algorithm as implemented in the scaled LMDER routine in MINPACK [49]. The values for $\beta$ and $\gamma$ are fixed so that the fitting routine does not fall into nonphysical minima. Should this happen the FA would show a preference for specific values of the phase, which result in inaccurate timing.

The final approach uses the weighted average of the trace. This algorithm will be referred to as the Weighted Average Algorithm (WAA), and the equation is given by

$$\phi = \frac{\sum_{i=\alpha}^{\beta}(y_i - \bar{b})i}{\sum_{j=\alpha}^{\beta}(y_j - \bar{b})}. \tag{2.3}$$

The parameter $y_i$ is the value of the trace at bin i or j, $\bar{b}$ is the average value of the baseline of the trace (see Figure 2.1), $\alpha$ is the starting bin for the weighted average, and $\beta$ is the final bin for the weighted average. The values for $\alpha$ and $\beta$ are chosen to optimize the resolution of the system.

Each of the methods described perform timing in the subsampling frequency range. The DCFD and the WAA are possible to implement on-board the digitizers, whereas the FA is much too complicated and requires post processing of the traces. One must take care that the algorithms are behaving as one would expect from the properties

of the digital system. To that end, we propose a method that confirms the behavior of the algorithms.

This method relies on the measurement of the time difference between two signals input into the electronics. The first signal has a phase $\phi_1$ and the second signal has a phase $\phi_2$. The delay ($\Delta$) between the signals is varied in intervals smaller than the sampling frequency of the digitizer to ensure the signals do not sample the same phase space. With a $\Delta$ of n times the sampling frequency, a bias of the timing algorithm would be impossible to detect. The measurement of the time difference for the three algorithms are shown in Figure 2.2. For a 0 ns delay between the signals (top row), all three of the algorithms produce similar results. This is due to the fact that the delay is equal to an integer multiple of the sampling frequency. Yet, once the $\Delta$ moves to 2 ns the DCFD fails to produce a single peak for the time difference indicating that the algorithm is suffering from bias when determining $\phi$. The FA and the WAA both produce a single peak for this delay.

The start and stop phases follow a linear relationship given by

$$\phi_1 = \phi_2 - \Delta. \tag{2.4}$$

due to the nature of the test setup, and with $\phi_1$ random with respect to the sampling clock. A plot of $\phi_1$ vs. $\phi_2$ immediately indicates the accuracy of the algorithm. A nonlinear relationship reflects deficiencies in the timing algorithm. Figure 2.3 displays the phase-phase diagrams for the three timing algorithms (columns). The first row in the figure uses $\Delta$=0 ns and all of the algorithms display linear results, as one would expect from Figure 2.2. The bias of the DCFD becomes rapidly apparent in Panel (f) of Figure 2.3, where the strict linear behavior of the system is not maintained. Both the FA and the WAA maintain the linear relationship regardless of the delay between the signals. In each of the graphs, the short lines appearing at 8 ns separation from the main distribution represent cases where the two signals have different filter clock timestamps.

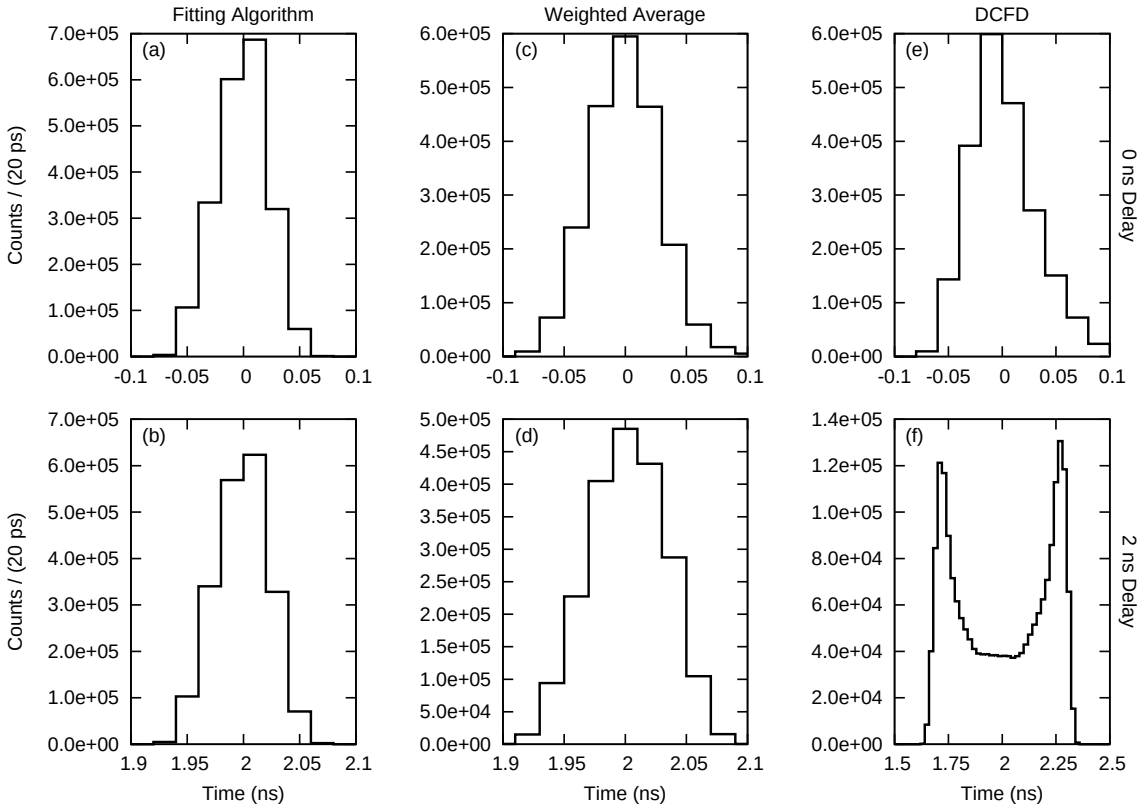


Figure 2.2: The resolutions of the various timing methods (columns) for two different signal delays, 0 ns (top row) and 2 ns (bottom row), at a signal amplitude of 1 V. The FA and WAA both produce a well defined peak for both delays. The DCFD fails to reproduce the proper timing when the delay between signals moves to 2 ns.

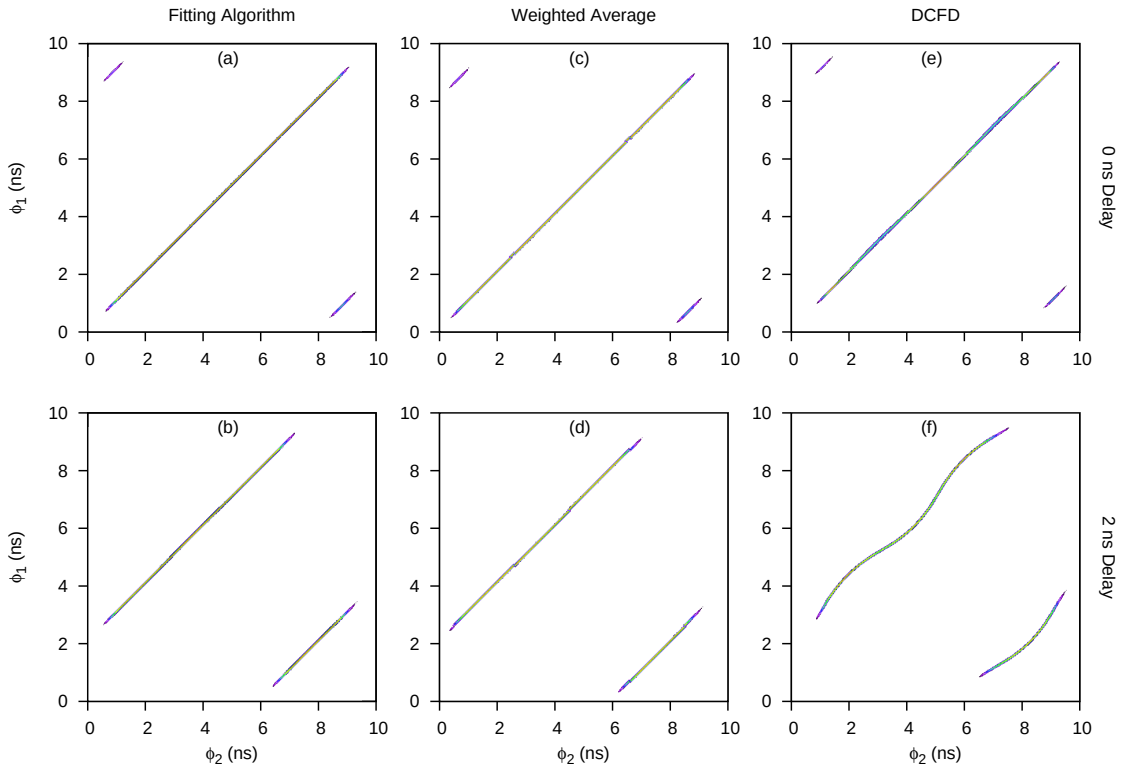


Figure 2.3: The phase-phase diagrams of the various timing methods (columns) for two different signal delays, 0 ns (top row) and 2 ns (bottom row), at a signal amplitude of 1 V. The DCFD do not behave according to the strict linear relationship. The small lines appearing at 8 ns from the main distribution are cases where one of the signals has a different timestamp.

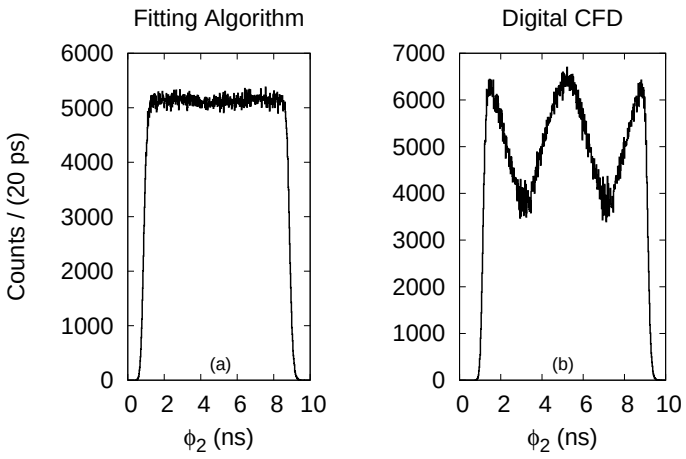


Figure 2.4: The projection of the phase-phase diagrams for the FA and the DCFD, each case is for $\Delta = 2$ ns. The FA does not show any bias in the phase space, where as the DCFD is heavily biased because the response of the function is nonlinear in the interpolation region. The WAA produces a projection similar to that of the FA.

In addition to the linear relationship between phases, one expects that the algorithm does not show bias towards a specific region of the phase space. This would be evidenced by spikes in the distribution of the phase-phase diagrams. Figure 2.4-(a) shows the projection of the phase-phase diagram for the FA with 2 ns delay (Fig. 2.3-(b)), and Figure 2.4-(b) is the projection for the DCFD (Fig. 2.3-(f)). One notices immediately the differences between the two methods. The distribution for the FA is flat, as one would expect from the random nature of the start signal, and this result is similar for the WAA. On the other hand, the DCFD shows bias toward specific regions of the phase space. The additional requirement of non-bias in the phase space provides a further confirmation that the algorithm behaves as expected.

The DCFD produces nonlinear results due to the use of a linear interpolation to extract the zero crossing. The derivative of the DCFD waveform determines the accuracy of the DCFD algorithm, and in the studied cases the derivative is nonlinear for fast signals [47]. For these types of signals, the DCFD would produce more accurate results using a faster digitizer, which would achieve local linearity around

the zero crossing. The FA explicitly takes into account the nonlinear nature of the trace by attempting to reproduce the proper response function for the signal. In the case that one leaves all of the FA parameters free to vary, the results are identical to those of the DCFD due to the highly non-linear nature of the phase sampled by the assumed response function. The FA and WAA, due to the preservation of the linear relationship between the two phases bear further investigation.

## 2.4 Performance With An Arbitrary Function Generator

### 2.4.1 Setup

The resolution of the two systems (100 MS/s and 250 MS/s) was studied for values of $\Delta$ ranging between 0 and 4 ns, and the resolution is given by the FWHM of the distributions, seen in Figure 2.2 and is denoted by $\xi$. The sensitivity of the resolution to the amplitude of the input signals was studied in a range of 20 mV to 1 V. The signal-to-noise ratio (SNR) for the 1 V signals was 64 dB for both the systems decreasing to 30 dB for the 20 mV signals.

In all cases, the FA calculated the proper $\Delta$ and the phase-phase plots remained linear. The biggest difference between the two systems can be seen in the behavior of the resolution as a function of the amplitude of the input signal. As seen in Figure 2.5, the resolution of the 100 MS/s system degrades quickly below 400 mV reaching a value of 1.7 ns for 20 mV signals. For 400 mV and above the 250 MS/s system yields a factor of 2 improvement in the resolution of the system. The largest gain in performance comes for the lowest amplitude signals where a factor of 3.5 is gained.

Similar tests were performed for the WAA for both digitization frequencies. The WAA again maintained the proper phase-phase relationship across all amplitudes and delays. For an optimized choice of averaging window, the WAA performs similarly to the FA. The WAA maintains a resolution of less than the sampling time over the

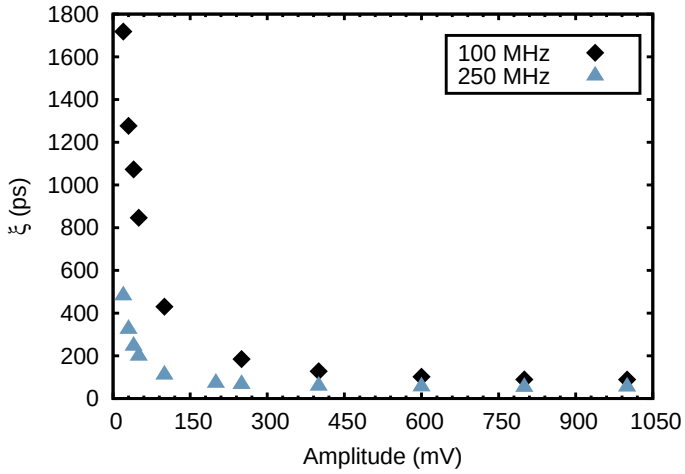


Figure 2.5: Time resolution as a function of input voltage for signals from the Tektronix 3102C Arbitrary Function generator using the Fitting Algorithm. The error bars are smaller than the point size.

full range, see Figure 2.6. Again, the 250 MHz system outperformed the 100 MHz system, leading to a factor of 2.7 improvement at 20 mV.

The WAA while having slightly worse resolution than the FA, 71 ps and 51 ps at 1 V respectively, has an advantage in that it can be relatively easily implemented in a digital system, e.g. on the DSP, which performs floating point operations. This would alleviate the need to store the digitized signals, thus increasing the throughput of the system. In addition, the WAA is more robust than the DCFD when processing fast signals. Due to the poor performance of the WAA for low amplitude signals, a resolution of 1 ns at 20 mV, with the studied systems only the FA is considered for applications to scintillator signals.

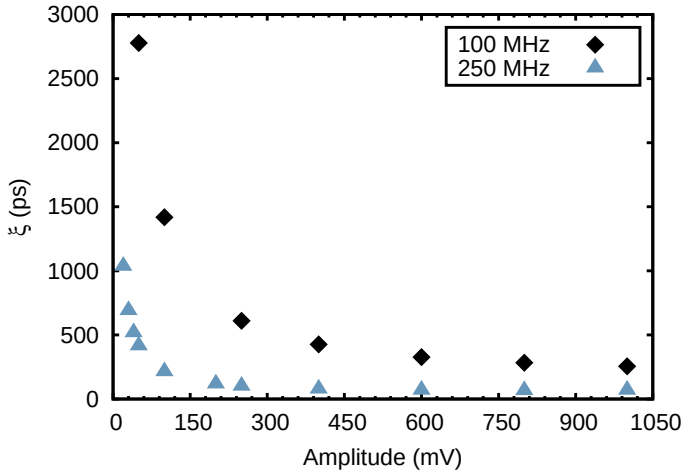


Figure 2.6: Time resolution as a function of input voltage for signals from the Tektronix 3102C Arbitrary Function generator using the Weighted Average Algorithm. The error bars are smaller than the point size.

# Chapter 3

# The Versatile Array of Neutron Detectors at Low Energy

The Versatile Array of Neutron Detectors at Low Energy (VANDLE) [50] detects neutrons and measures their energy via the time-of-flight (ToF) technique. The ToF technique uses the time difference between two detectors in order to measure the amount of time required for the particle of interest to cover a known distance. Using this information one may calculate the energy of the particle. Even though this is a conceptually simple technique it is one of the easiest and most powerful methods for measuring neutron energies [39, 40, 41, 42, 51].

By design, VANDLE is versatile, meaning that it can achieve a variety of scientific goals at many different experimental conditions. There are currently two major configurations of the array, seen in Figure 3.1. One of these configurations is optimized for beta decay experiments; the other is used for reaction experiments. These configurations can be changed and adapted to fit into the spacial requirements of the facility at which an experiment will be run. More importantly, these designs are adapted so that VANDLE may be used in conjunction with other detector systems. Most notably, during the experiments discussed in Chapter 5, VANDLE was coupled

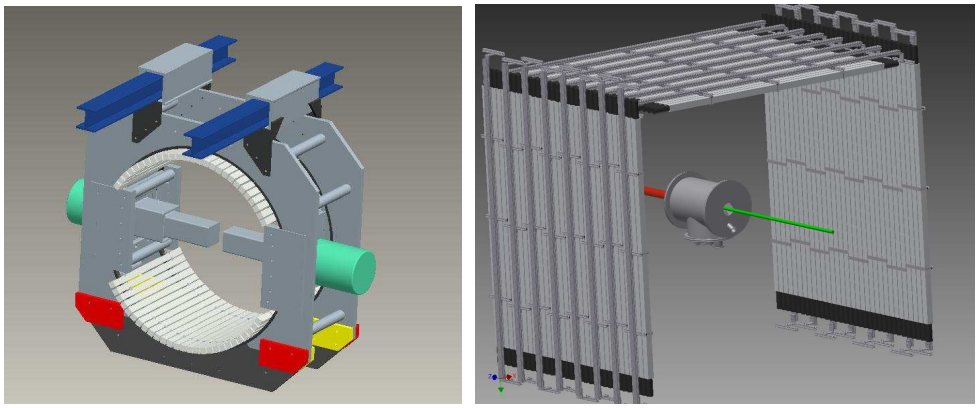

(a) $\beta_n$ configuration (b) (d,n) configuration

Figure 3.1: VANDLE in the two main configurations.

with a high purity germanium detectors that provided the ability to perform $\beta - \gamma$-neutron correlations.

A fully digital data acquisition system provides VANDLE with several integral features. First is low energy neutron detection thresholds. This is accomplished using a coincidence triggering scheme that is fully implemented on the acquisition board. The low threshold triggering means that it is possible to detect neutrons with energies of 100 keV or lower and run the system in the photomultiplier's thermal noise. Details of this triggering scheme are discussed in Section 3.5. Second, the timing for the system is better than 1 ns for photomultiplier (PMT) signals. This is discussed further in Section 3.4. VANDLEs modular design necessitates a unique characterization for each module. This characterization involves gain matching the modules so that they behave identically to the same incident light. This process is discussed in Section 3.3.

## 3.1 Scintillator Theory

VANDLEs detector material is composed of plastic scintillators. Plastic scintillator materials come in a wide variety of forms and are used in many applications due to

their versatility. These scintillators are amenable to production in large quantities, and can be shaped into various geometries. This means that they are relatively cheap, making them ideal for large detector arrays that require a large coverage area.

Scintillators produce light (fluoresce) when a particle strikes atoms within the material. This causes atomic excitations, which then decay via the release of photons. An important feature of scintillators is that they must be "blind" to their own scintillation light. Thus, the energy required for the excitation of the atoms is generally much higher than the emission light. In many scintillators, the deexcitation of the atoms is on the order of picoseconds, which gives rise to signals with fast response times suitable for timing purposes.

The amount of light that is produced inside the scintillator is proportional to the energy deposited by the incoming particle or photon. In addition, the light produced changes depending on the type of incident particle. To standardize the light yield from scintillators one uses the unit MeV electron equivalent (MeVee). The unit is related to the amount of light that an electron deposits in the scintillator. For example, 1 MeVee of light will be generated by an electron with energy 1 MeV for a given scintillator material; however, a 1 MeV neutron will generate only a fraction of 1 MeVee of light [52].

As discussed by J. B. Birks [53], a particle incident on the scintillator will leave a path of damaged molecules. These damaged molecules will quench the light produced and cause the overall light production in the scintillator to temporarily decrease. The fluorescence can be described as a function of the incident particle energy and the penetration depth by the equation:

$$\frac{dS}{dr} = \frac{A\frac{dE}{dr}}{1 + kB\frac{dE}{dr}}. \tag{3.1}$$

The term $dS/dr$ describes the fluorescence, $AdE/dr$ describes the excitations along the particle track, $BdE/dr$ is the concentration of damaged molecules along the path, and $k$ is the probability that damaged molecule will quench the light [54, 55]. In

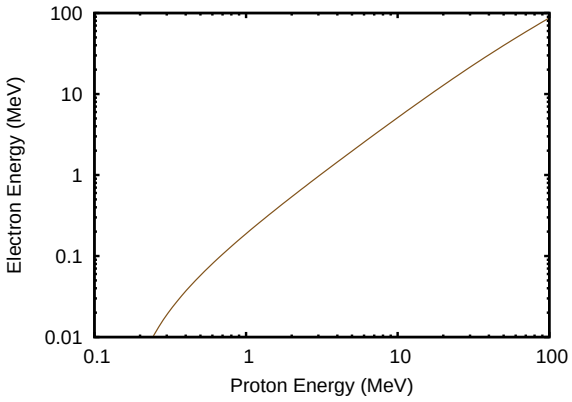


Figure 3.2: The electron energy (light output) as a function of the incident proton energy for the scintillator material used in VANDLE.

practice, the parameter $A$ is known, and the parameter $kB$ is fit to experimental data. For VANDLEs scintillator material this equation has been parameterized by Madey et al. [56], the graph of the electron energy (light output) as a function of proton energy is shown in Figure 3.2.

As light travels through the scintillator it will lose intensity or attenuate. The attenuation of the light can be expressed as

$$\frac{I}{I_0} = e^{-x/L}. \tag{3.2}$$

I is the intensity of the light at position x, $I_0$ is the amount of light initially emitted, and L is the attenuation length [52]. The attenuation length for the VANDLE bars is measured to be longer than the length of the module. Therefore, more than 63% of the emitted light reaches the ends of the module. As discussed in the previous chapter, the timing of the acquisition system depends on the amplitude of the input signal, and it is imperative that a significant fraction of the emitted light be collected to improve the timing and low energy threshold for the module.

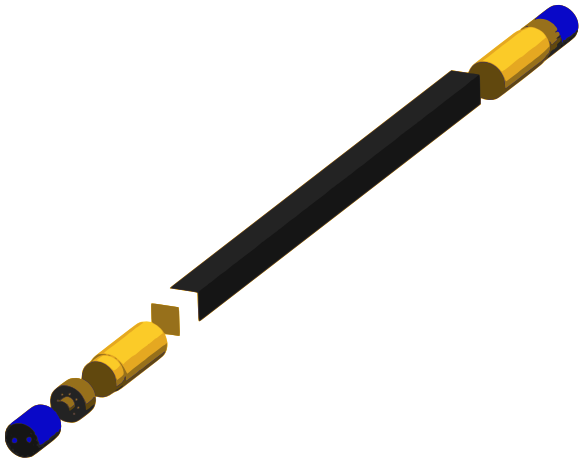

Figure 3.3: The schematic diagram of a single VANDLE module. The black component represents the scintillator material. The yellow, brown, and blue components depict the photomultiplier tube, the voltage divider, and the end cap, respectively.

## 3.2 Physical Assembly

VANDLE uses square scintillator bars. Two sizes were chosen to achieve the full breadth of the scientific goals. A schematic of a single VANDLE bar is shown in Figure 3.3.

The first size is a 3x3x60 $cm^3$ bar. Due to their size, the "small" bars have small light attenuation, which provides sensitivity to low energy neutrons, on the order of 100 keV. They are efficient at detecting neutrons with energies greater than 100 keV. These reasons make the small bars an excellent choice for studying beta-delayed neutron emission. These experiments typically require detection of neutrons with a broad energy range. A particular challenge is the detection of low energy neutrons emitted from states near the neutron separation energy.

The "large" bars have dimensions of 5x5x200 $cm^3$. The larger size allows for a larger solid angle, which means that the bars can be placed much farther from the implantation point. The added thickness means that the bars are sensitive to a much higher range of neutrons (2-20 MeV) than their smaller counterparts. These bars have a similar intrinsic efficiency as the small bars; however, the peak of the

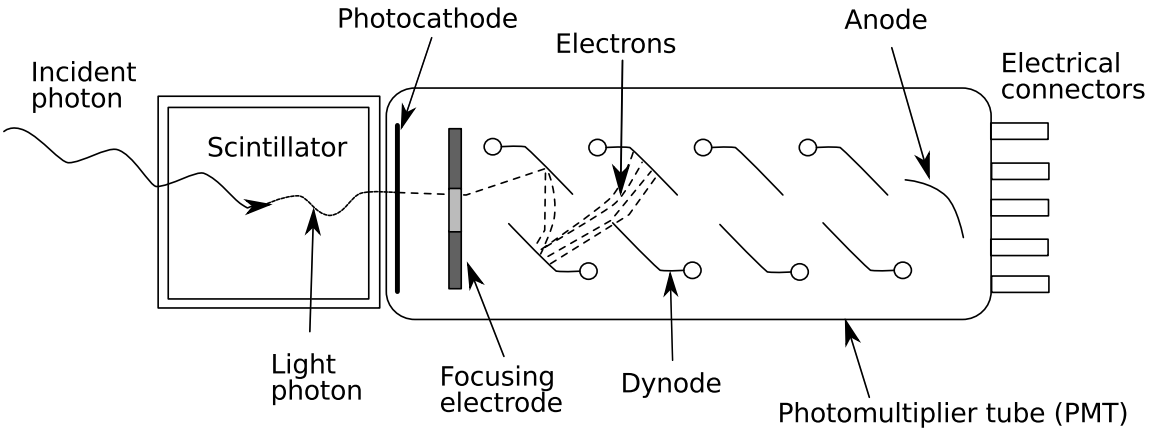


Figure 3.4: A schematic of a photomultiplier tube with attached scintillator. The dashed lines indicate the path of the electrons.

efficiency curve is higher in energy, nearly 2 MeV. The size and energy coverage give these bars an advantage in reaction studies where one expects a range of neutron energies depending on the detection angle.

### 3.2.1 Photomultiplier Tubes

Scintillator detectors typically require a photomultiplier tube (PMT) to convert scintillation light into electrical signals. The conversion takes place in several steps, see Figure 3.4. First, the scintillation light impinges on the photocathode, which converts the photons into electrons. This conversion occurs through the photoelectric effect. The most common types of photocathodes are semiconductors; the type is chosen to match the frequency of scintillation light. Electrons from the photocathode pass into the electron collection optics. This focuses the emitted electrons into the electron multiplier. The electron multiplier consists of many dynodes, which are designed so that the electric fields between them accelerate electrons from the previous dynode toward the next. The accelerated electrons strike the next dynode in the sequence at a few hundred eV and strike with enough energy to release secondary electrons [57]. Immediately following the final dynode is an anode that collects the electrons released in the electron multiplication stage. The anode not only collects

the electrons but also makes a connection to the output electronics. In most cases the output electronics consists of a voltage divider that serves two purposes: providing connections for biasing the PMT and outputting the signal from the anode.

Each VANDLE module has a PMT on each end, see Figure 3.3. This configuration allows for optimal light collection. If only a single PMT were used, events at the far end of the scintillator would have little of their light reach the PMT due to the light attenuation. This would produce fewer electrons in the photocathode, and a smaller output signal. The timing of the system depends upon the amplitude of the signals; it is critical to maximize the amount of light collected in the PMTs.

### 3.2.2 Wrapping Material

There are two layers of wrapping material on the scintillators. The inner layer serves to keep the scintillation light from escaping the scintillator. The timing performance of the detector is linked with the amount of light that can be collected from the scintillator. Various wrapping materials were tested to judge their effectiveness at reflecting the scintillation light. Nitrocellulose paper (nitro) had the best performance, followed by aluminized Mylar. Unfortunately, the nitro is expensive and brittle. For a large detector array the cost of will be prohibitive. The brittleness makes working with large quantities of the material difficult. For these reasons, only the small bars are wrapped in the nitro. In contrast the Mylar is relatively cheap, and easy to work with making it the ideal choice to wrap the larger bars.

The outer layer of the wrapping material provides several benefits. First, it protects the inner layer of wrapping. This is especially important for the nitro due to its fragility. Second and most important, the outer wrapping prevents external light from entering the detector. If the outer layer of wrapping is not light tight, a variety of problems can arise. The PMTs may be damaged as they serve to amplify light that reaches them. The external light drastically increases the amount of background that the PMTs experience, which makes distinguishing true scintillation light from

the external light difficult, if not impossible. To complete the wrapping, a piece of shrink tubing is placed over the PMTs. The tubing provides extra stability to the joint between the PMT and scintillator. It has an added effect of providing another layer of light protection at the ends of the bars were the wrapping materials may not fully cover.

## 3.3 Gain Matching

Gain matching is the process by which one calibrates individual PMTs so that they respond identically to the same incident light ensuring uniformity between different VANDLE modules. This is a critical step in the characterization of the modules. If the bars are not gain matched, then one cannot create composite data by summing the individual bars together. In addition, gain matching provides an energy calibration for the light output of the detectors. In this way, one can adjust the response of the detectors to fit the specific needs of the experiment.

In practice, one uses the Compton effect to gain match the PMTs. A source is placed at the center of a VANDLE module ensuring that the light reaching both PMTs is the same. The gammas from the source scatter off electrons in the plastic. The energy of the recoiling gamma is calculated by

$$E'_\gamma = \frac{E_\gamma}{1 + \frac{E_\gamma(1-cos\theta')}{m_e c^2}}. \tag{3.3}$$

From which it follows that the maximum energy of the electron will be when the gamma transfers the maximum energy or when $\theta' = \pi$.

$$E'_\gamma = \frac{E_\gamma}{1 + \frac{2E_\gamma}{m_e c^2}} \tag{3.4}$$

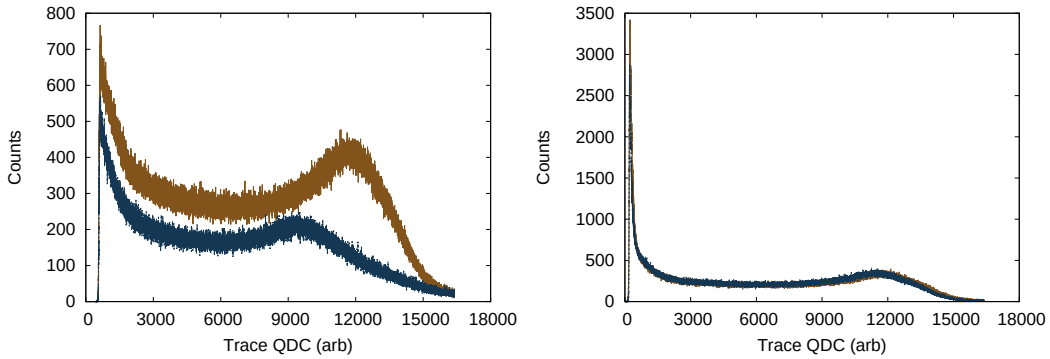


(a) Before Gain Matching (b) After Gain Matching

Figure 3.5: (a): The integrated trace values (QDC) before the PMTs are gain matched. (b): The integrated trace values (QDC) after the PMTs are gain matched.

The energy of the electron can be calculated from the following expression:

$$E_e^{max} = E_\gamma - E'_\gamma. \tag{3.5}$$

The electron energy is expressed in keVee. The energy of the electron can be used to calculate the light output of the scintillator. This can yields the conversion between ADC channel and keVee. By appropriately setting the position of the Compton edge in the ADC one can ensure that the ADCs dynamic range encompasses the entire range of neutrons of interest.

Figure 3.5a displays the individual PMTs for a single module before gain matching. The two PMTs have the same applied voltage, but perform differently for the same incident light. Figure 3.5b shows the same bar after the gain matching has been done. The two PMTs now behave identically to the source. The difference in statistics is due to a difference in measurement times.

## 3.4 Teeny VANDLE

The application of the FA to a pulser is an idealized situation. To determine the response of the algorithm to a true photomultiplier signal, a pair of test detectors was

constructed. The detectors used small 1x1x0.4 $in^3$ pieces of Eljen EJ-200 scintillator coupled to Hamamatsu R580 PMTs from VANDLE. The length of the scintillator crystal contributes approximately 80 ps to the time resolution, given by the transit time of light through the small scintillator chip. The components were arranged into two configurations. The first used a single piece of scintillator material between two PMTs. This detector is optimized for measuring the timing of the system. The second arrangement, optimized for the measurement of timing walk, uses two scintillators each with their own PMT. In each case the scintillator and PMTs were wrapped in a layer of Teflon tape, a layer of Mylar with polymer backing, and black electrical tape.

The resulting detectors were connected to the Pixie-16-250 system in the same setup as the pulser. A $^{60}$Co source provides a calibration for the PMT. The Compton edge of the source was placed at 75% of the ADCs dynamic range. This means that a majority of the signals will be of high amplitude and as seen in Figure 2.5, they will produce the best possible timing. More details of the specific setups follow in the next sections.

### 3.4.1 Resolution

The results of the resolution test can be seen in Figure 3.6. This resolution is the time difference between the arrival times of the PMTs attached to the small piece of scintillator. The resolution of the system is approximately 0.6 ns over the full range. If only the high energy signals are considered the resolution improves to approximately 0.5 ns. The resolution will be dominated by the transit time of the electrons in the PMTs and not by the algorithm. This detector also maintains the linear relationship between the phases, Figure 3.7. Both this and the resolution indicate that the FA performs as needed for high resolution timing purposes.

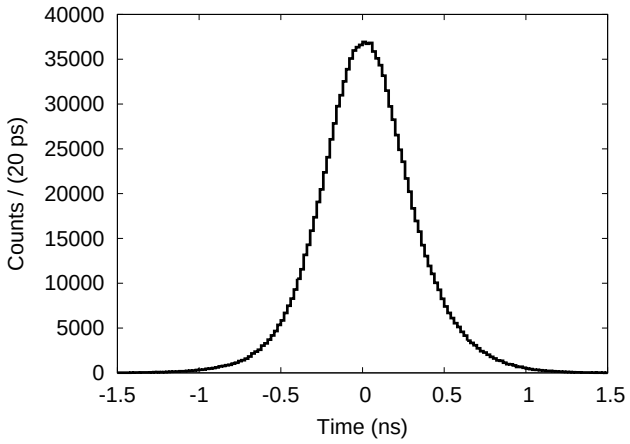


Figure 3.6: The time difference between two PMTs in the resolution setup. These signals were analyzed using the Pixie-16-250 setup. The full width at half max is 0.625 ns.

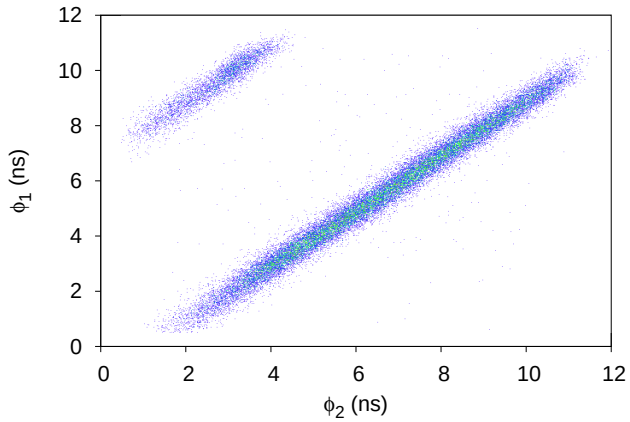


Figure 3.7: The phase-phase diagram for the small scintillator detector. The width of the lines is due to the 0.7 ns resolution of the detector. They display the proper linear relationship for timing from the digital system.

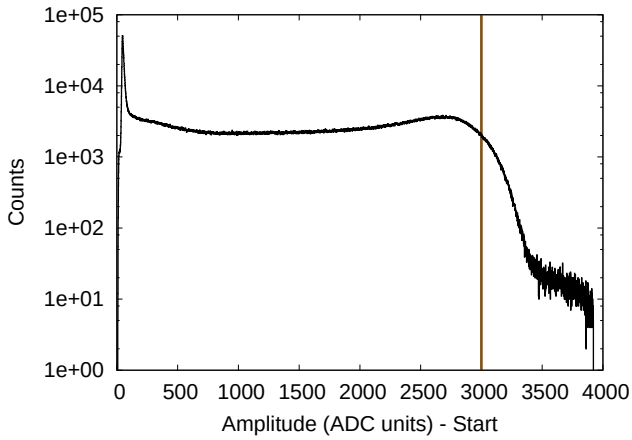


Figure 3.8: The amplitude of the start signal. The vertical line represents the software threshold for plotting the Max Amplitude of the stop versus the time difference, Figure 3.9.

### 3.4.2 Timing Walk Characterization

This measurement used two detectors each consisting of a scintillator coupled to a PMT. The detectors are independently wrapped and timing walk of the system occurs when the relative amplitudes of the signals are mismatched. To measure the timing walk, we use a software gate on signals with amplitude larger than the Compton edge associated with the gamma source, see Figure 3.8, and have minimum timing walk. After this condition is imposed the amplitude of the second signal is plot against the time difference between signals, see Figure 3.9. Cuts on the amplitude for the second signal are made, which project the time difference. This projection is fit with a Gaussian function, and one can construct a graph of the walk as a function of amplitude, see Figure 3.10. A fit applied to these data provides a way to correct the calculated phase.

## 3.5 On-board Triggering Logic

In addition to the digital timing methods, we developed a custom triggering scheme for VANDLE. This triggering scheme allows the system to operate at a low energy

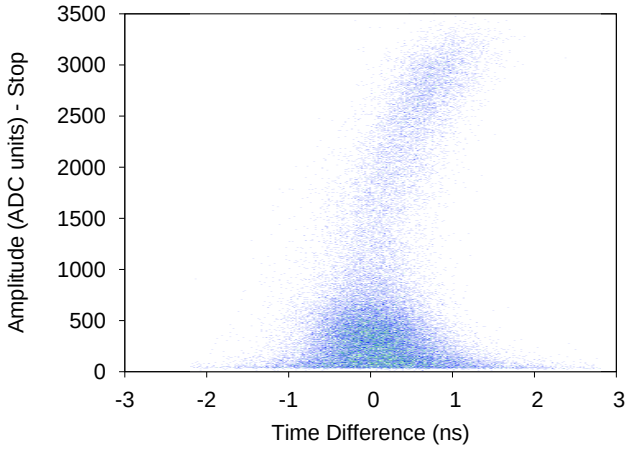


Figure 3.9: The amplitude of the stop signal vs. Time Difference for the walk characterization. The start signal is gated on traces that have amplitudes greater than the Compton edge of the source, Figure 3.8.

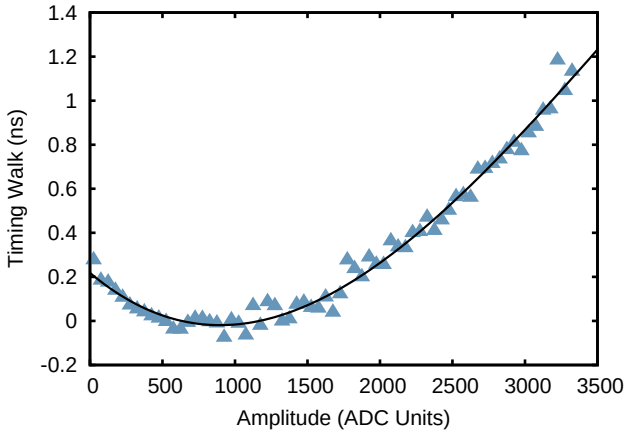


Figure 3.10: The timing walk as a function of signal amplitude. The line indicates the fit to the data.

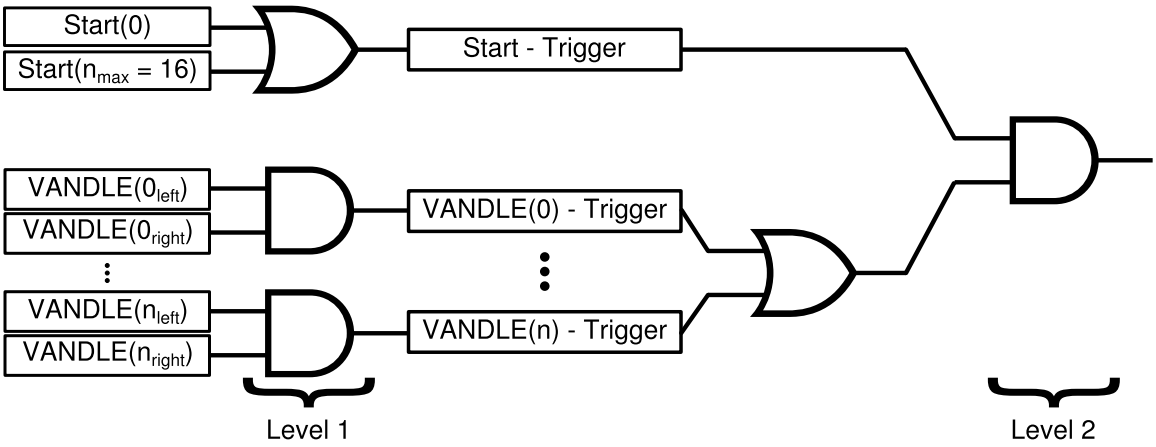


Figure 3.11: A schematic of the on-board coincidence triggering used for the VANDLE system. Level 1 indicates the pairwise coincidences between PMTs on a VANDLE module. Level 2 represents the logical AND condition between VANDLE and the start detectors. The system can handle up to 16 start detectors and n VANDLE modules.

threshold while reducing data rates. The triggering scheme, while following standard practices implemented for similar detectors, is unique in that it does not use auxiliary electronics to distribute the implementation across the FPGAs of the data acquisition system. The diagram, Figure 3.11, is the schematic representation of the logic gates implemented on the FPGAs. The FPGAs generate the coincidence signals via the on-board logic filters using operating principles developed previously for a segmented germanium detector array [58].

Implementing pairwise coincidences for the PMTs on each VANDLE module provides sensitivity for low energy signals from neutrons, Level 1 in Fig. 3.11. This operation is implemented locally, as each pair of signals use the same FPGA. The coincidence condition of 100 - 200 ns reduces the readout rate and is sufficient to nearly eliminate triggers on thermal noise. The pairwise triggering increases the neutron efficiency due to the greatly lowered trigger thresholds, more details on this will be discussed in a subsequent publication [34].

The local coincidence condition is not completely adequate for VANDLEs needs as VANDLE is a time-of-flight detector. This means that VANDLE requires an auxiliary

"start" detector, and this start detector must be considered in the full coincidence triggering scheme. The triggers generated by the signals from the start detector are distributed through the backplane bus to all of the FPGAs in the system [58]. As is shown in Fig. 3.11, Level 2 is a logical AND between VANDLE and the start triggers that has a broader time gate, 1 $\mu$s long and takes into account the spread in the time of flight. The output of this gate is broadcast back to the trigger bus and seen by all FPGAs and used for validation of the triggers. In this situation the acquisition records only signals that have at least one pair of VANDLE signals and a start detector. The specific detectors producing the start signals varies between experiments: a beta detector for beta-delayed neutron studies or a trigger associated with a specific nuclear reaction. The reliable operation of this coincidence scheme was tested with 3 MHz on the start trigger, which fulfills the requirements for VANDLEs data acquisition. The versatility of the on-board coincidence triggering, as well as the reduced data load, is instrumental to the performance of the digital acquisition system.

## 3.6 Efficiency of Neutron Detection

Because every particle passing through the scintillator does not deposit energy, the most important feature of the detector to characterize is the efficiency. The efficiency allows one to determine the absolute number of undetected particles during a measurement. In order to determine the efficiency, a comparison must be made to a standard with a known efficiency. In this work two methods provided an independent check of the efficiency of a VANDLE module.

The first method used the $^{27}$Al(d,n) reaction measured by Massey et al at Ohio University [59]. This reaction produces a continuous neutron spectrum in the range of 0.2 and 14 MeV; the precise range of interest for VANDLE. A tandem accelerated deuterons to an energy of 7.4 MeV, which were then incident on an $^{27}$Al target. Pulsing the beam of deuterons provided a start signal for the acquisition system.

A movable arm, holding the target, allows the angle of the reaction products to be adjusted. The neutron spectrum of interest required an angle of 120°. A large concrete wall with an aperture collimated the neutrons and gammas from the reaction.

The small VANDLE module, placed 13 m from the reaction target, had two measurement positions. The first position placed the module so that the beam of neutrons and gammas illuminated the entire scintillator. The second position positioned the VANDLE module above the beam, and provided a measurement of the background. With the VANDLE module in this position, no neutron events correlated with the beam pulses. The efficiency measured in this experiment are shown in Figure 3.12

The second method of calibration uses neutrons emitted from a $^{252}$Cf source. The neutrons from this source are characterized and the results summarized by Manhart [60]. This experiment required a reference detector in order to determine the absolute yield of neutrons from the source. The LENDA group used an identical detector in the efficiency calibration for their scintillators [42]. A comparison of the spectrum from the liquid scintillator and from the VANDLE module provides a measurement of the efficiency, see Figure 3.12. The two methods for measuring the efficiency agree well. This provides VANDLE with a well characterized response.

## 3.7 Detector Simulations

Simulations of the detector modules are necessary to understand aspects of the system, which may be difficult or impossible to measure. For example, during a typical beta decay experiment in the absence of a normalization case; the absolute number of neutrons produced cannot be determined. A simulation of the full detector setup will allow one to reconstruct the expected efficiency. The simulation provides crucial information about the modules and systems that may otherwise be unattainable.

The Geant4 [61] provides the framework necessary to perform simulations for this work. This software package allows one to build each component of the detector,

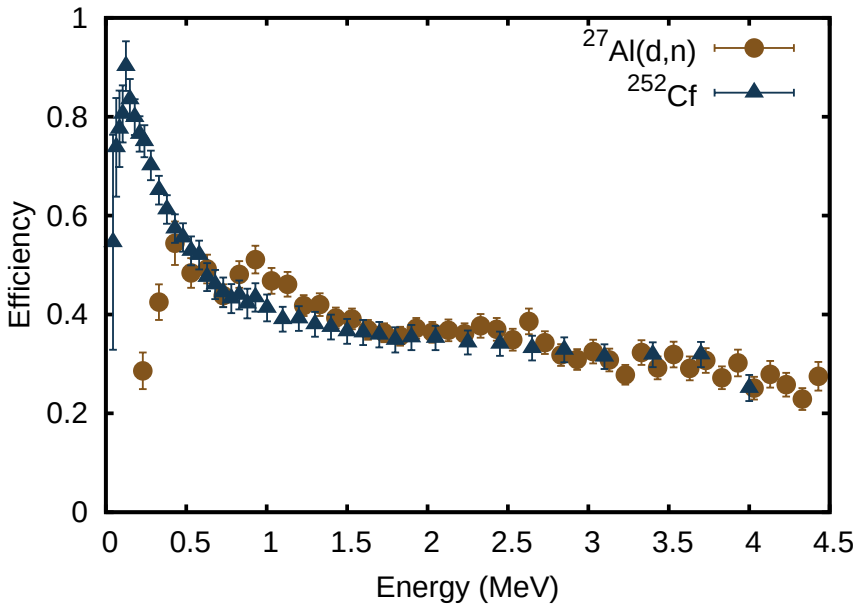


Figure 3.12: The efficiency for the small VANDLE module using the $^{27}$Al (d,n) reaction (circles) and $^{252}$Cf (triangles). The threshold for the $^{27}$Al(d,n) data was 30 keVee, and the threshold for the $^{252}$Cf measurement was 0 keVee.

experimental setup, and surrounding environment. Once this is complete, the user can then choose from a variety of radiation sources to interact with the environment. The user may specify the type of radiation and the geometry of the source. The software then proceeds to run Monte Carlo events for the desired setup and provides the user with visualization options.

The results from the simulation are only as good as the implementation of the necessary physics. It is, consequently, critical for one to test the simulation against measured or known quantities. Only in this way will one achieve a robust simulation. This work uses the measured efficiency as a benchmark for the simulations. The results of this comparison are shown in Figure 3.13. This figure demonstrates that the simulation of the VANDLE modules contains the necessary physics to reproduce accurately the detector's response.

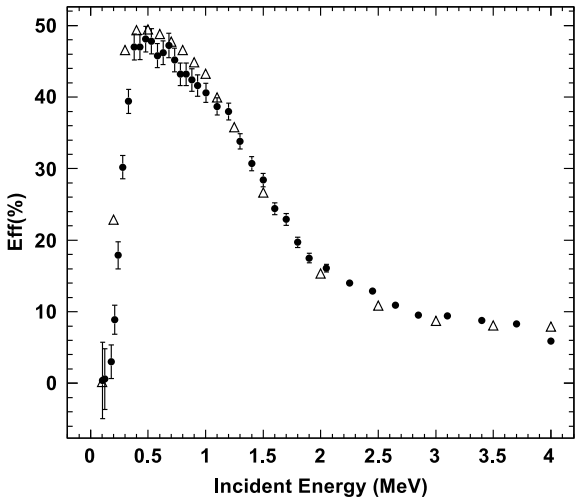


Figure 3.13: The simulated efficiency (diamonds) compared with the measured efficiency from a $^{252}$Cf measurement. The threshold for this simulation was 30 keVee.

# Chapter 4

# Beam Production and Experimental Details

## 4.1 The Hollifield Radioactive Ion Beam Facility

The Hollifield Radioactive Ion Beam Facility (HRIBF) [62], Figure 4.1 at the Oak Ridge National Laboratory uses the isotope separation on-line technique [63] to produce rare, unstable isotopes. The Oak Ridge Isochronous Cyclotron produces a beam of 40 MeV protons, which impinge on a Uranium Carbide target. The protons induce fission in the target, which is heated so that the fission fragments effuse from the ion source cavity where they are surface ionized [64]. An electric field extracts the ions and accelerates them towards the mass separators. The first stages of mass separators separate various elements according to their mass number.

The beam then passes into a charge exchange cell that creates negative ions. Negative ions are necessary for use with the tandem accelerator. After the charge exchange cell, the beam passes through a final stage of isobar separation. This stage of separation is capable of creating a nearly pure beam of the desired isotope. Finally, the beam is transported to the experimental end station [65].

Figure 4.1: A schematic view of the HRIBF.

## 4.2 The Low-energy Radioactive Ion Beam Spectroscopy Station

The Low-energy Radioactive Ion Beam Spectroscopy Station (LeRIBSS) [66], Figure 4.2 is used to study the decay of neutron rich isotopes. LeRIBSS receives radioactive ion beams from the high resolution isobar separator magnets. Because the tandem accelerator is not used, the beams can either be positively or negatively charged. This allows for higher beam rates because the charge exchange cell used to produce negative ions has an efficiency between 10 and 50% [65].

### 4.2.1 Electrostatic Kicker and Moving Tape Collector

The ions are implanted onto a 1/2 inch tape that is part of the moving tape collector. The moving tape collector is coupled to a electrostatic kicker that deflects the beam away from the implantation point. One detection "cycle" is a period of beam

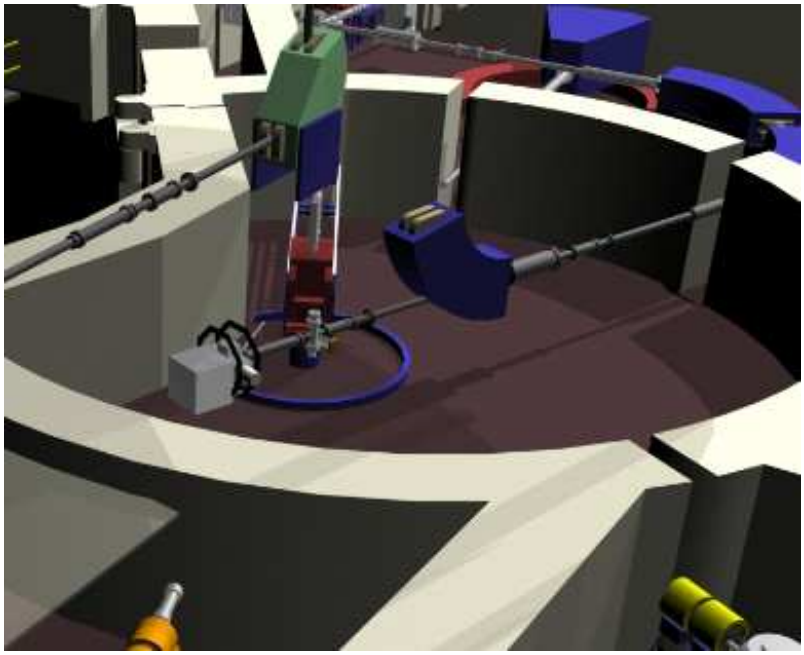

Figure 4.2: A schematic of LERIBSS, which is located directly below the tandem tower in Figure 4.1.

collection on the film, a period where the beam is deflected by the kicker, and a period where the decay products are transported away from the detectors. The cycle is adjusted for the specific isotope of interest. For example, if the isotope of interest has a half-life of 0.5 s. A possible cycle would be 3 s, 2 s, and 0.6 s. This would allow the isotope of interest to reach saturation, meaning that the implantation rate is the same as the decay rate. The decays would then be observed for 4 half-lives. The sample would be then moved away from the detectors in 0.6 seconds. Figure 4.3 displays a typical grow-and-decay curve for the neutrons from $^{77}$Cu, the measured half-life of the decay is 0.52(0.01) s, which is slightly larger than the expected 0.4681(20) s.

### 4.2.2 Beta Detectors

To detect the beta particles emitted during $\beta^-$ decays a pair of 1 mm thick plastic scintillators surround the implantation point, see Figure 4.4. The 1 mm thickness provides a reduced interaction probability for gamma rays in the scintillator. These

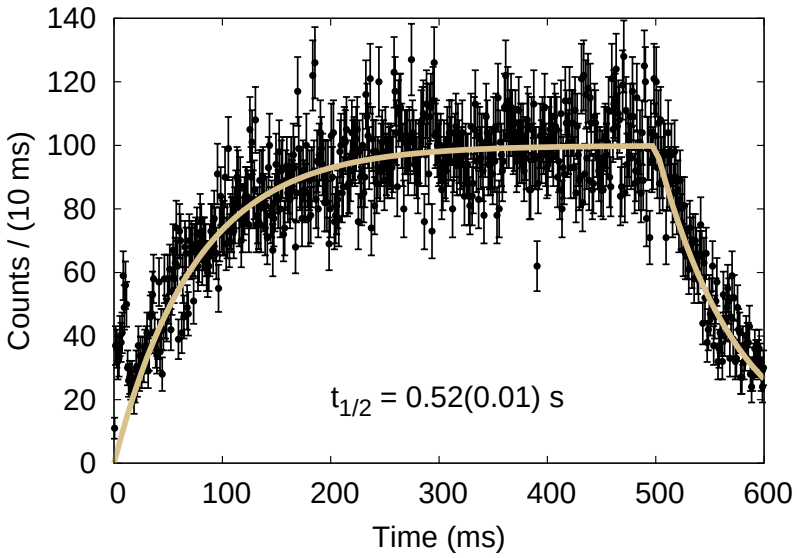


Figure 4.3: The grow-and-decay curve for the neutrons from the decay of $^{77}$Cu. The measured half-life is 0.52(0.01)s.

scintillators are curved so that they completely surround a 2 inch diameter beam pipe. The light attenuation of such a thin scintillator is high, which means that particles interacting at the far end of scintillator have a small fraction of their light reach the PMT. These scintillators require the use of a light guide, which bend the light from the thin interface of the scintillator to the circular aperture of the PMT. The typical efficiency of these detectors ranges from 13% to 60%, and depends upon the electron energy. The efficiency curve for the beta scintillators is presented in Reference [67].

### 4.2.3 High Purity Ge Clover Detectors

The experimental setup used two Ge clovers. The clovers measure the gamma rays emitted from the $\beta^-$ decay critical for the identification of isotopes. The gamma rays can be used to create gates on neutrons detected in VANDLE. Therefore, it is imperative that the efficiency and calibration of the Ge detectors be determined. This procedure is well known, and will not be detailed here, for more information see Refs. [52, 68]. The efficiency curve for the clovers is shown in Figure 4.5.

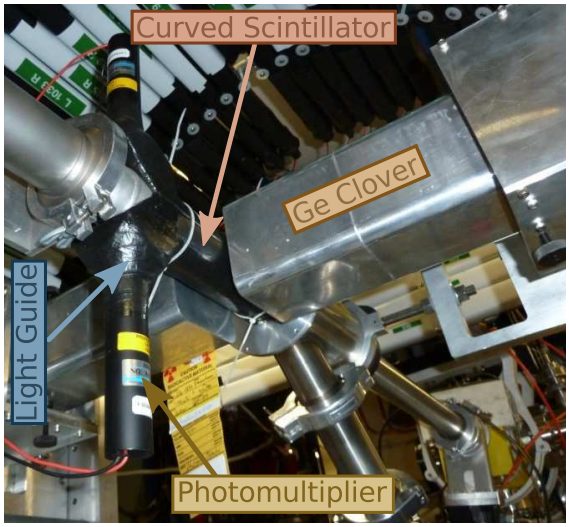


Figure 4.4: A photograph of the beta scintillators and clovers. The individual components are labeled. The implantation point is located between the Ge clovers.

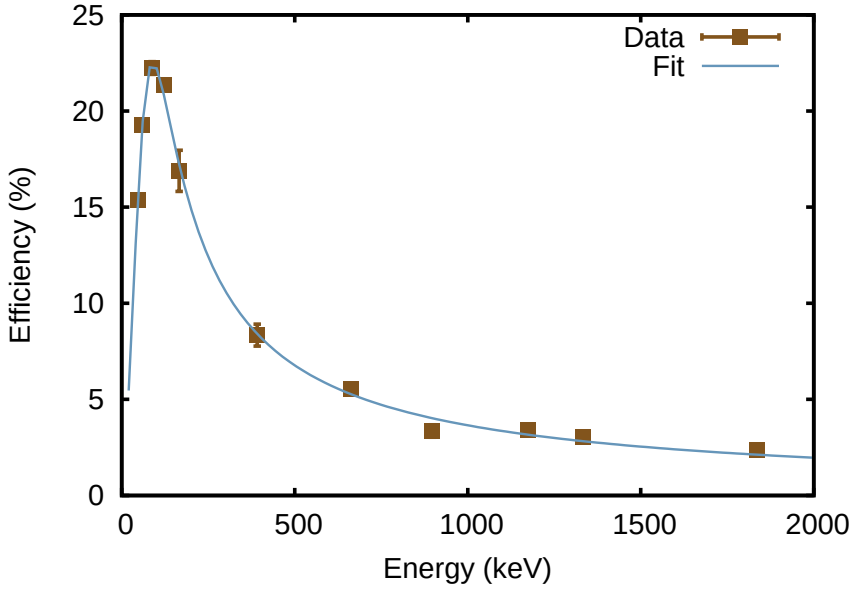


Figure 4.5: The efficiency curve for the Ge clovers. The squares represent the data points, the blue line the fit to the data.

# Chapter 5

# Experimental Analysis

The analysis of VANDLE data is broken into several stages. The ultimate goal of the analysis is the reconstruction of the neutron intensity from the ToF spectra. The analysis begins with constructing a simulation of the experiment. Next, one sorts the data and constructs the necessary information to begin the visualization. The final stage of the analysis is the reconstruction of the experimental B(GT) from the neutron spectra. Each of these steps are detailed in the following sections.

## 5.1 GEANT4 Simulations and Efficiency

GEANT4 simulations of the experimental setup (Fig. 5.1) are critical to the analysis because neutrons scatter from the experimental setup and other detectors. VANDLE modules detect these scattered neutrons at times longer than direct neutrons giving peaks in the ToF spectrum a tail at longer times of flight, see Figure 5.2. These peak shapes provide the basis for fits to the ToF spectrum.

The neutron detection efficiency for VANDLE varies depending on the threshold of the cuts imposed on the data. Because there is not a simple way to directly measure this, we use a GEANT4 simulation to determine the efficiency as a function of the varying threshold. A plot of this efficiency is shown in Figure 5.3.

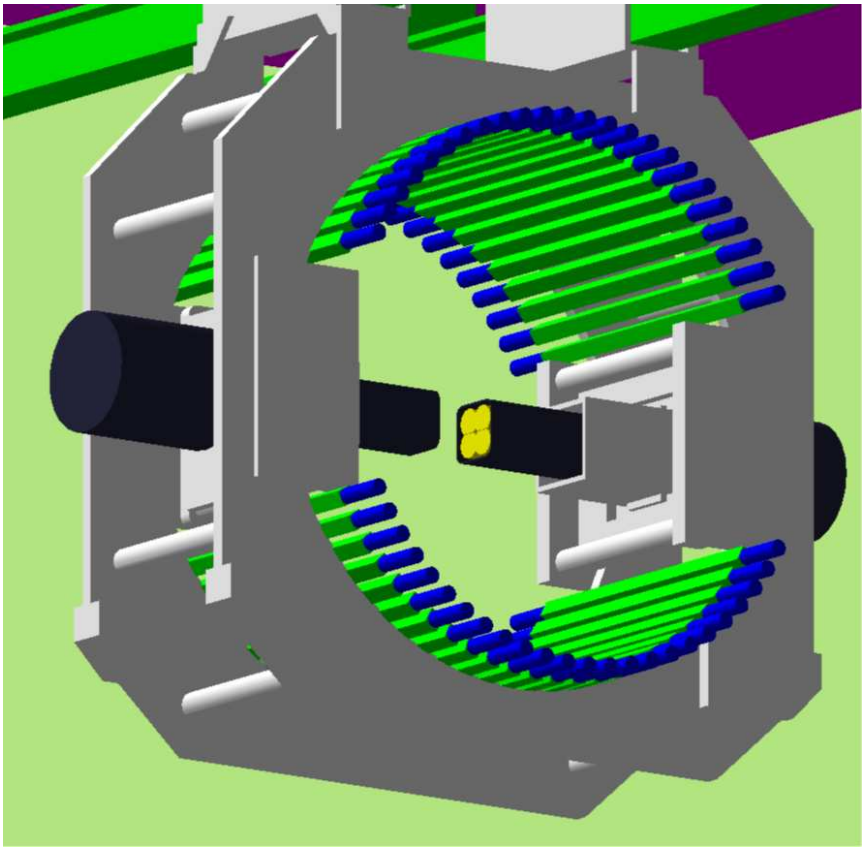

Figure 5.1: The experimental setup as modeled in GEANT4. Picture courtesy S. Ilyushkin.

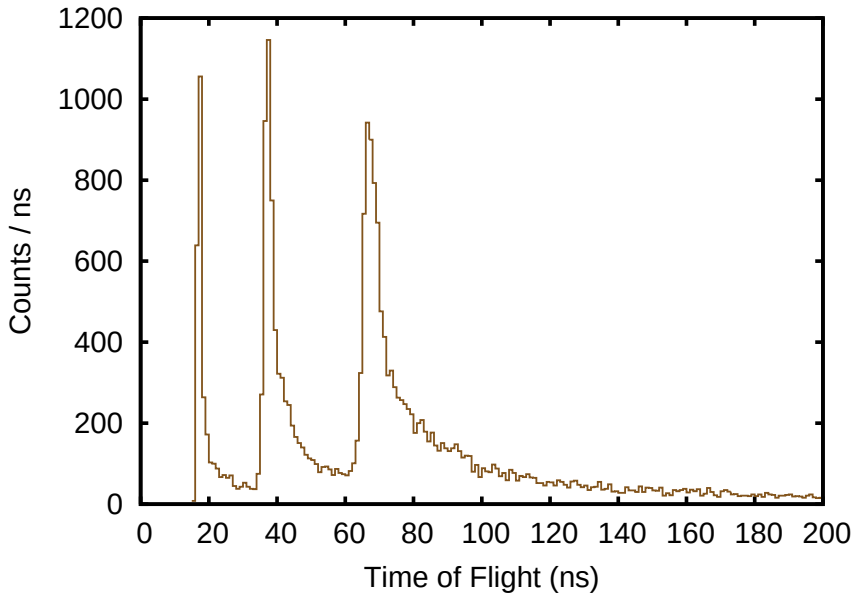


Figure 5.2: The effects of scattered neutrons on the neutron peaks as modeled by the GEANT4 simulation. The simulation takes into account the corrections to the ToF introduced by the neutron flight path.

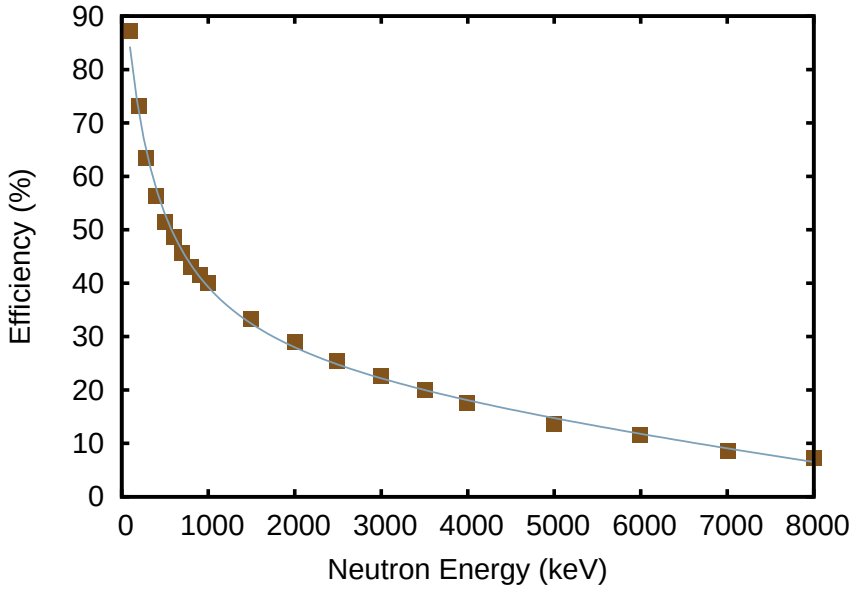


Figure 5.3: The intrinsic neutron detection efficiency of a single VANDLE module from the GEANT4 simulation using a threshold imposed by the banana cut in Figure 5.4. The solid blue line is a fit to the data points, which come from the simulation of the setup.

## 5.2 Data Parsing

The first step parses raw data from the Pixie modules into an "event" according to a user defined event window. For this experiment, the event window was chosen to be 3 $\mu$s; any events with time differences inside of the three ns window are considered correlated. A C++ program sorts the events according to the timestamp and applies the timing algorithms discussed in Chapter 2. The program also applies the various energy and time calibrations to the data. Then the events are analyzed according to their detector type, e.g. individual VANDLE modules are "built". This stage of the analysis correlates the $\beta$, gamma, and neutron events, and performs gating of the data. Due to the high amount of scattering in the system, only a subset of the VANDLE bars are used for this analysis. Once the data is sorted it is passed to the visualization routines.

## 5.3 Visualization

### 5.3.1 Neutron Time-of-Flight Spectra

As each event is processed by the software, the data fills user defined histograms, see Figure 5.4. This figure plots the light output (L) of a VANDLE module as a function of the time of flight (ToF) of the detected particle. The prompt gammas from the decay appear at a ToF of 1.7 ns. Because the neutrons deposit a range of energies into the scintillator they may be identified by their kinematic curve, which follows the kinetic energy formula, ($E = 0.5mv^2$). The banana gate (blue line) in Figure 5.4 acts as a veto for events lying outside the banana and one may project the spectrum onto the ToF axis. Figure 5.5 displays the ToF spectrum for $^{77,78}$Cu and $^{84}$Ga.

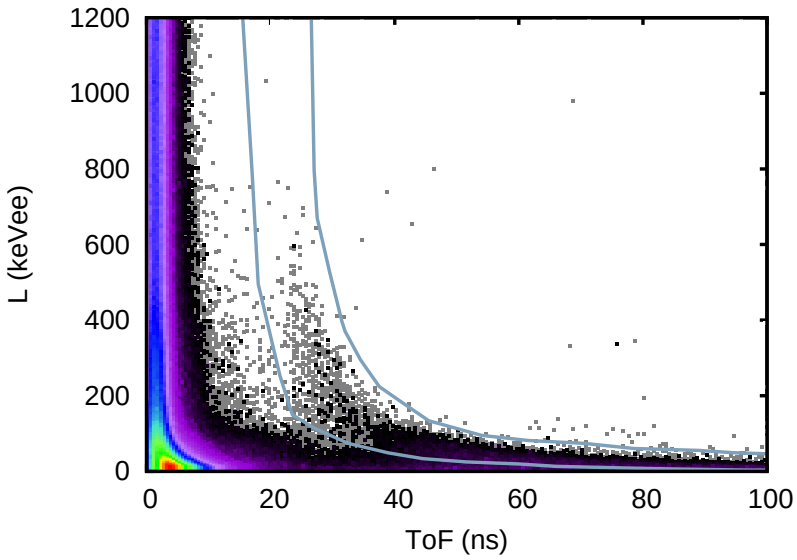


Figure 5.4: The light output versus time of flight for $^{77}$Cu. The large peak at 1.7 ns corresponds to the prompt gammas from the decay. The blue line is the banana gate and outlines the neutron kinematic curve.

### 5.3.2 Ge Clover Spectra

The Ge clovers play two instrumental roles in the experiment: beam identification and neutron gating. Beam identification is possible due to the fact that each nucleus posses a characteristic gamma spectrum, see Figure 5.6. In this figure, the top most brown line represents an ungated gamma spectrum. The blue line demonstrates the effects of applying a coincidence condition with the $\beta$ detectors, which remove background contaminants, e.g. $^{40}$K. This spectrum provides a precise view of the nuclei that are associated with a beta particle. The final tan line in Fig. 5.6 displays the effect of neutron gating on the gamma spectrum, the banana gate provides this coincidence condition.

The two gammas in Fig. 5.6a, 598.6 keV and 697.7 keV, originate from the $4^+ \rightarrow 2^+ \rightarrow 0^+$ cascade observed by Ilyushkin et al. [67] in the decay of $^{77}$Cu. For the decay of $^{78}$Cu, Fig. 5.6b, a single line survives the neutron gating with energy of 114.7 keV, previously observed by Korgul et al. [69]. Similarly, a single line survives in the $^{84}$Ga spectrum, Fig. 5.6c, with an energy of 247.8 keV. None of the presented cases

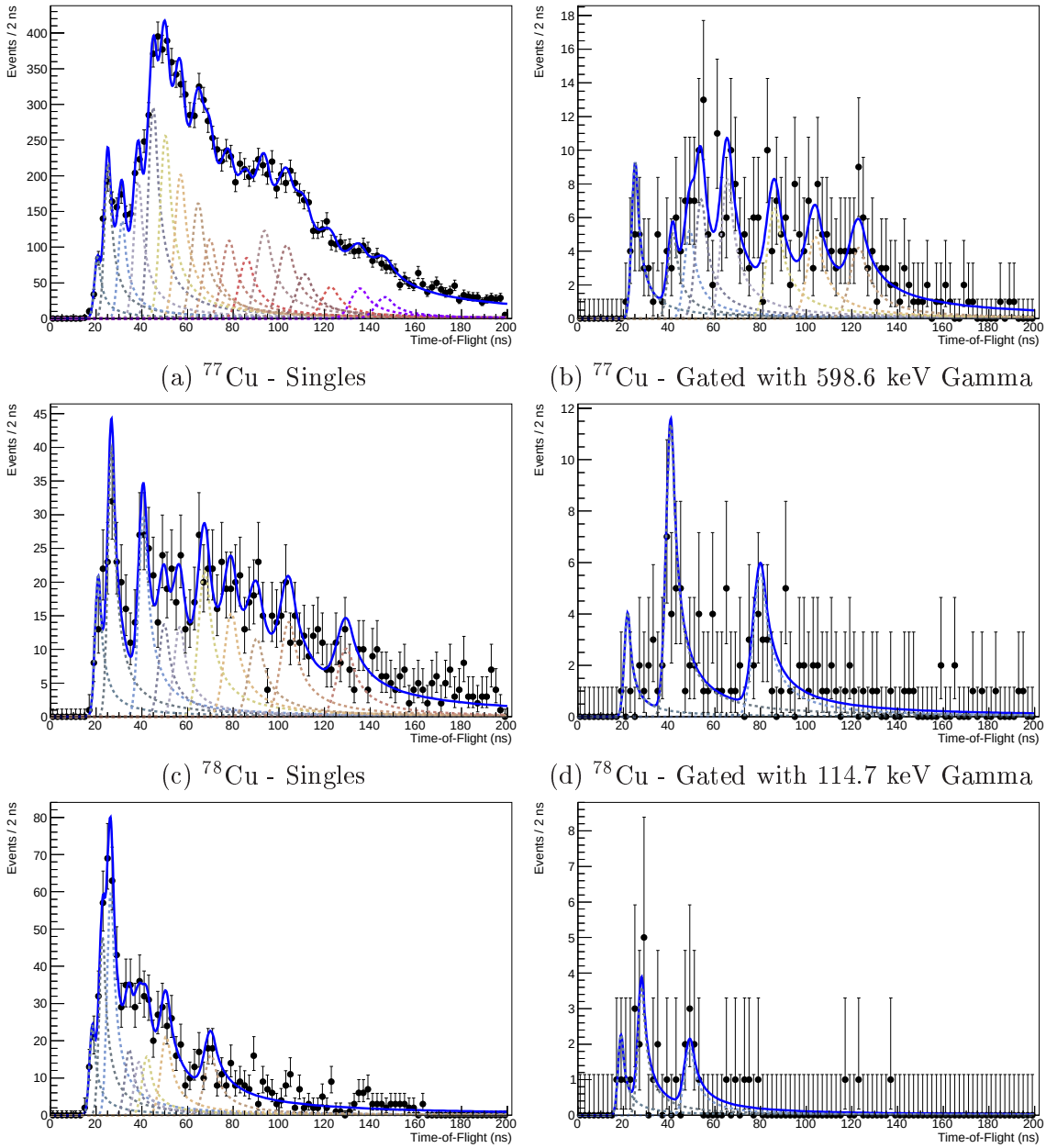


(a) $^{77}$Cu - Singles

(b) $^{77}$Cu - Gated with 598.6 keV Gamma

(c) $^{78}$Cu - Singles

(d) $^{78}$Cu - Gated with 114.7 keV Gamma

(e) $^{84}$Ga - Singles

(f) $^{84}$Ga - Gated with 247 keV Gamma

Figure 5.5: The ToF spectra for $^{77,78}$Cu and $^{84}$Ga. The blue line is the results from the ML fit to the data (points). The dashed curves below the blue curve are the individual Crystal Ball components of the fit. In panels (b), (d), and (f) the neutron spectrum has been gated on the indicated gamma transition in the beta-delayed neutron daughter.

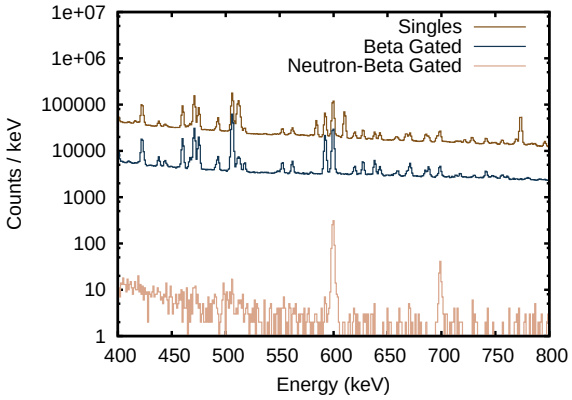


(a) $^{77}$Cu

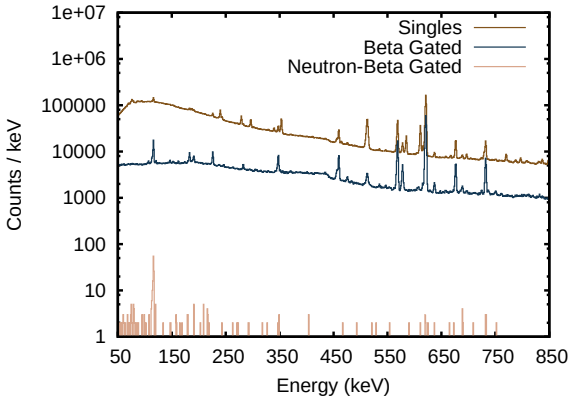


(b) $^{78}$Cu

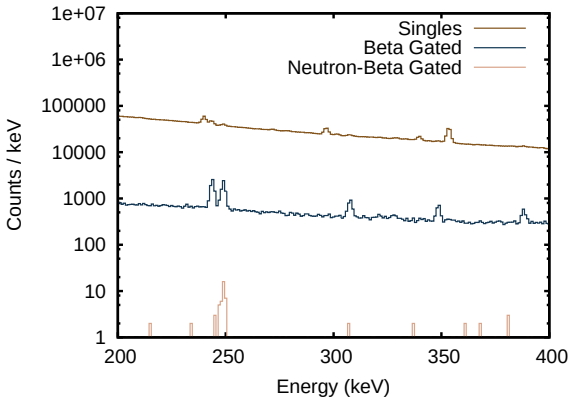


(c) $^{84}$Ga

Figure 5.6: Gamma spectra for $^{77,78}$Cu and $^{84}$Ga. The brown line represents the gamma singles spectrum. The blue line displays the beta gated gammas, and the tan line shows the beta-neutron gated gammas.

display an unknown gamma line in coincidence with the neutrons. These gammas lines play a pivotal role in understanding the structure of the decay.

The gammas associated with the neutron spectra provide additional gating for the previous Neutron spectra. Gating on gamma lines from the beta-delayed neutron daughter provides information about the the emitted neutrons, such as their spin. Figure 5.5 displays the neutron spectra gated using the gammas associated with deexcitation of the beta-delayed neutron daughter. One may immediately notice differences between the singles spectra, e.g. Fig. 5.5c, and the gated spectra, Fig. 5.5d; the gamma gated spectra may display only peaks at particular neutron energies. The drawback to gating the neutron spectrum using the gammas is that one may be left with low statistics, see Fig 5.5f.

### 5.3.3 The VANDLE Analysis Software Toolkit - VAST

The final stage in the data workflow has been bundled into the VANDLE Analysis Software Toolkit (VAST). This toolkit provides the necessary C++ software to fit the ToF spectra, calculate the neutron branching ratio, and calculate the B(GT). This software was developed so that the analysis of ToF data from VANDLE could be processed easily and efficiently. These steps are discussed in the following sections.

### 5.3.4 Maximum Likelihood Fitting

The ToF data were analyzed using maximum likelihood fitting. This fitting method uses probability density functions (PDFs) to determine the parameters of an analytic function that were most likely to produce the provided data set. This fitting method does not require the data to be binned into a histogram, thus making it more robust by removing any dependence on the binning of the data. This method works well for data sets with low statistics, because a least-squares algorithm requires that the individual histogram bins obey Gaussian statistics [70].

Here we adopt the notation used by Myung [71]. Let $f(\hat{y}|\hat{w})$ denote a PDF which yields the probability of observing the data $\hat{y}$ given the set of parameters $\hat{w}$. Each data point in the data vector is assumed to be statistically independent from one another. Under this assumption, one writes the PDF as

$$f(\hat{y}|\hat{w}) = \prod_{j=1}^{N} f_j(y_j|w_j). \tag{5.1}$$

The PDF must be a continuous, differentiable function. This is a crucial requirement as the function is maximized through differentiation during the analysis.

In general, one knows the data making up y, and is interested in finding the functional parameters that reproduce it. For this work, a Crystal Ball (CB) function [72, 73, 74] closely approximates the detector response. The CB has a Gaussian core, which is modified by a power-law tail, see Eqn 5.2.

$$f(x;\alpha,n,\mu,\sigma) = N \cdot \begin{cases} e^{-(x-\mu)^2/(2\sigma^2)}, & for \frac{x-\mu}{\sigma} > -\alpha \\ A * (B - \frac{x-\mu}{\sigma})^{-n}, & for \frac{x-\mu}{\sigma} < -\alpha \end{cases} \tag{5.2}$$

Where,

$$A = \left(\frac{n}{|\alpha|}\right)^n e^{-|\alpha|^2/2} \tag{5.3a}$$

$$B = \frac{n}{|\alpha|} - |\alpha| \tag{5.3b}$$

$$N = \frac{1}{\sigma(C+D)} \tag{5.3c}$$

$$C = \frac{n}{|\alpha|} \cdot \frac{1}{n-1} \cdot e^{-|\alpha|^2/2} \tag{5.3d}$$

$$D = \sqrt{\frac{\pi}{2}} \left(1 + erf\left(\frac{|\alpha|}{\sqrt{2}}\right)\right) \tag{5.3e}$$

The power-law component of the CB takes into account neutrons scattered from materials surrounding the detectors arriving at much later times, see Figure 5.2. The

sigma of the CB should account for both the intrinsic timing of the VANDLE module, as well as the resolution of the start detector. This resolution of the start detector is obtained by fitting the prompt gammas in the ToF spectrum. The GEANT4 simulation of the experiment provides the intrinsic timing of a VANDLE module, which is dependent upon the energy of the incident neutron. The final PDF that is used will be a convolution of the Gaussian resolution from the start detector with a CB having an intrinsic resolution based off of its mean.

Now that a suitable PDF is identified, we now define the likelihood function, L. L is defined by inverting the roles of $\hat{y}$ and $\hat{w}$ in the PDF:

$$L(\hat{w}|\hat{y}) = f(\hat{y}|\hat{w}). \tag{5.4}$$

The likelihood function of interest will be the set of $\hat{w} = \{w_0, \ldots, w_k\}$ that reproduce the data in $\hat{y}$. The technique of maximum likelihood estimation (MLE) enables one to determine the set of $\hat{w}$ that is most likely to have produced the data. Taking the natural log of the likelihood function, ln $L(\hat{w}|\hat{y})$, makes the problem more computationally tractable. Maximizing the likelihood equation,

$$\frac{\partial \ln L(\hat{w}|\hat{y})}{\partial w_i} = 0, \tag{5.5}$$

with respect to the $w_i$ yields the MLE estimate. In addition, the condition must be met that the second derivative of the log likelihood function must be a maximum:

$$\frac{\partial^2 \ln L(\hat{w}|\hat{y})}{\partial {w_i}^2} < 0. \tag{5.6}$$

### 5.3.5 Implementation of the Maximum Likelihood Method

This work used the RooFit [75] package available within the ROOT [76] data analysis framework for performing the fits. RooFit uses the MINUIT [77] minimization algorithms to perform the fits. In order to take advantage of these algorithms the

RooFit package constructs the negative log-likelihood (NLL) function, -ln$L(w|y)$. This function is then minimized with respect to the free parameters of the function. Figure 5.5 displays the results of these fits; the individual fits shall be discussed later in this chapter.

It is necessary to parameterize the variables $\alpha$, n, and $\sigma$ in the CB function because they control aspects of the function that depend on the mean. The $\alpha$ parameter controls the fraction of the function contained within the tail. The parameter n controls how quickly the tail dies, and $\sigma$ is the resolution of the Gaussian. The parameterization occurs in three steps. First, the simulated data for a given neutron energy is fit with a CB shape. This fitted function is then convoluted with a Gaussian with the measured resolution of the beta detector. The parameters of the convoluted function provide the final parameters for the CB response function at the given energy. This process is repeated for various energies between 0.1 and 5 MeV to determine the functional dependence of the parameter on the neutron energy. These variables are then fully dependent upon the ToF during fits to the spectrum. This procedure has an added benefit in that the fitting algorithms no longer need to perform the convolution of the CB with the Gaussian on the fly.

Because the neutron peaks are, in general, unresolved, one must choose how many peaks to include in the model to reproduce the data. This can quickly lead to overfitting of the data set and erroneous results. A natural way to check the robustness of the fit is to generate a Monte Carlo sample from the fitted model, fix all of the fitted parameters except the yields, and fit the model to the MC data set. If a particular yield displays variations that do not follow Gaussian statistics with a mean of 0 and a variance of 1.0, it is likely that the model is over or underfitting the data set.

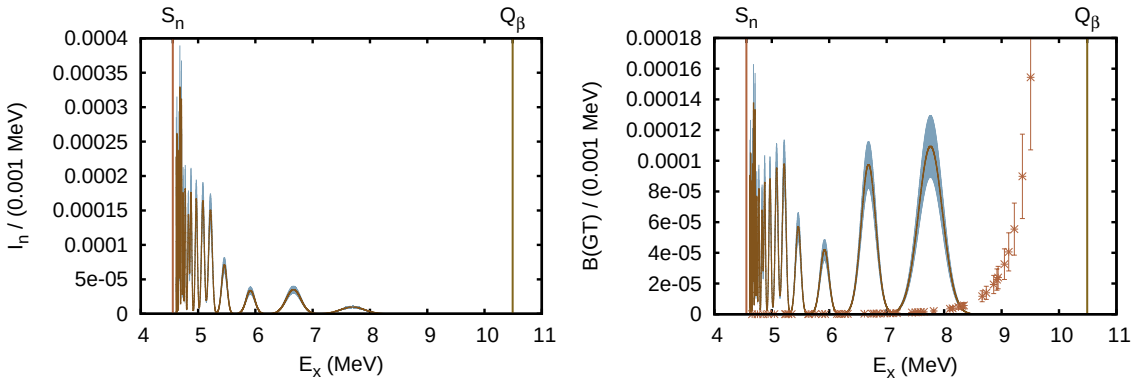


(a) $^{77}$Cu - Intensity




(b) $^{77}$Cu - B(GT)

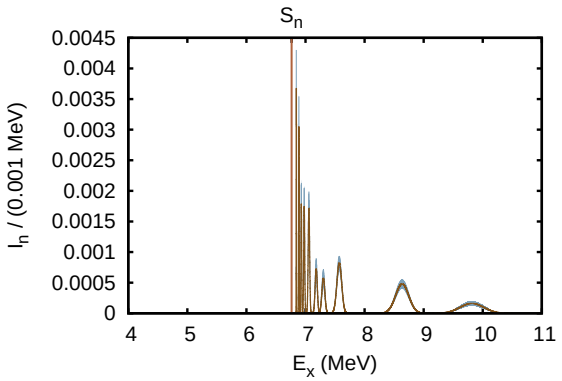


(c) $^{78}$Cu - Intensity

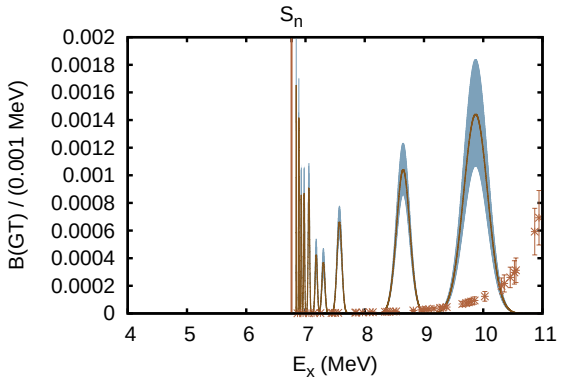


(d) $^{78}$Cu - B(GT)

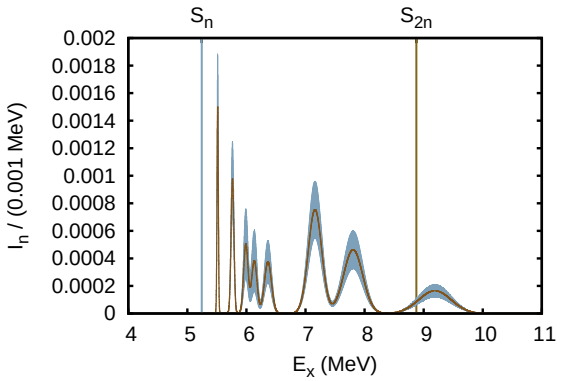


(e) $^{84}$Ga - Intensity

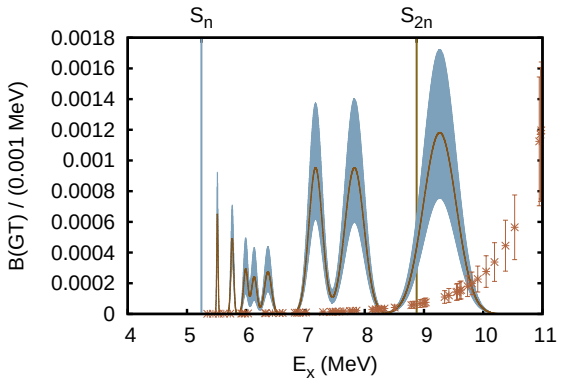


(f) $^{84}$Ga - B(GT)

Figure 5.7: The branching ratio spectra and B(GT) for $^{77,78}$Cu and $^{84}$Ga. The vertical lines represent the indicated neutron separation energies and Q value for the decay. These spectra assume that all of the neutron feeding goes to the ground state. The calculation includes spreading of the intensity due to the timing resolution of the system. The stars show the sensitivity limit of the system.

## 5.4 Calculation of the $P_n$ and B(GT)

The individual components of the fitted model only provide the yield within the fitted region. For this reason, it is necessary to integrate the tail of the components outside of the fitted region. The integrated area of the components is then adjusted by the intrinsic efficiency of the VANDLE modules, which provides the neutron yield ($Y_n$) for a given component (n). Summing the $Y_n$ for each component gives the total intrinsic efficiency adjusted yield for the model. The total number of decays may be calculated by the following equation:

$$N_\beta = \frac{A_\gamma}{\epsilon_\gamma I_\gamma}. \tag{5.7}$$

$N_\beta$ is the total number of beta decays, $A_\gamma$ is the total number of observed gammas for a particular gamma energy, $\epsilon_\gamma$ is the Ge efficiency for the measured gamma line, and $I_\gamma$ is the absolute branching ratio of the gamma line. Dividing the total number of neutrons by the total number of beta decays yields the $P_n$ for the decay.

The total neutron yields of the components also provide the branching ratio ($I_n$) of the neutron peak, which is given by

$$I_n = \frac{Y_n}{N_\beta \Omega \epsilon_\beta}. \tag{5.8}$$

$\Omega$ is the geometric coverage of the bars in the experiment, and $\epsilon_\beta$ is the efficiency of the beta scintillators. The branching ratio is then spread using a Gaussian distribution, where the amplitude is given by the magnitude of the branching ratio, the mean is the energy of the neutron peak, and sigma is given by $\sigma_{In} = 0.5\sigma_n$. The spreading provides the neutron density distribution seen in Figures 5.7a, 5.7c, and 5.7e.

Using the neutron density distribution, one may calculate the beta decay strength distribution, B(GT):

$$B(GT) = \frac{C}{f(Z, Q_\beta - E_x)(t_{1/2}/I_n)}. \tag{5.9}$$

The coefficient C is a constant with a value of 3812.4 s, $f(Z, Q_\beta - E_x)$ is the Fermi function, $E_x$ is the excitation energy of the neutron line, and $t_{1/2}$ is the lifetime of the decay, for a full derivation of this equation see Ref. [7]. Figures 5.7b, 5.7d, and 5.7f display the results of this calculation. There is a hard cutoff on the low energy side of the B(GT) at 0.03 MeV due to the banana gate. The stars on these Figures show the sensitivity limit of the measurement. Each star represents the B(GT) calculated from a neutron peak containing 10 measured neutrons. The background for the measurement is 1 count per second, which means that a neutron peak with 10 counts would be at the 10 sigma limit for the measurement. The sensitivity limit curve indicates that the measured B(GT) are statistically significant. The interpretation of the B(GT) follows in the next chapter.

# Chapter 6

# Experimental Results

The VANDLE experiment investigated nearly 30 nuclei, see Figure 6.1, around doubly magic $^{78}$Ni and $^{132}$Sn. These regions provided many excellent cases for beta-delayed neutron emission because they are near closed shells and far from stability. Little information is known on the energies of the neutrons emitted from these nuclei. Rudstam et al. used a $^{3}$He proportional counter to measure the energy spectra of various fission fragments and observe a discrete line structure in the spectra [27]. Similarly, Kratz et al. investigated As and Br isotopes using a $^{3}$He ionization chamber [28] and from these spectra calculated the beta decay strength distribution. These strength distributions and discrete line structures do not take into account the possible effects of pandemonium. Greenwood et al. performed one of the last measurements of beta delayed neutrons in the light fission fragment region using a combination of $^{2}$H detectors and a $CH_4$ ionization chamber [78]. Since this measurement in 1997 the study of energy resolved beta-delayed neutron emission of fission fragments has been stagnant and VANDLEs goal is to bridge this gap in the experimental data. The most recent measurements in this field are a remeasurement of the $^{137}$I precursor by Yee et al. [79].

The decay of isotopes near $^{78}$Ni may be schematically explained by the Extreme Single Particle Shell Model (ESPSM) [1] as a transformation of single particle neutron

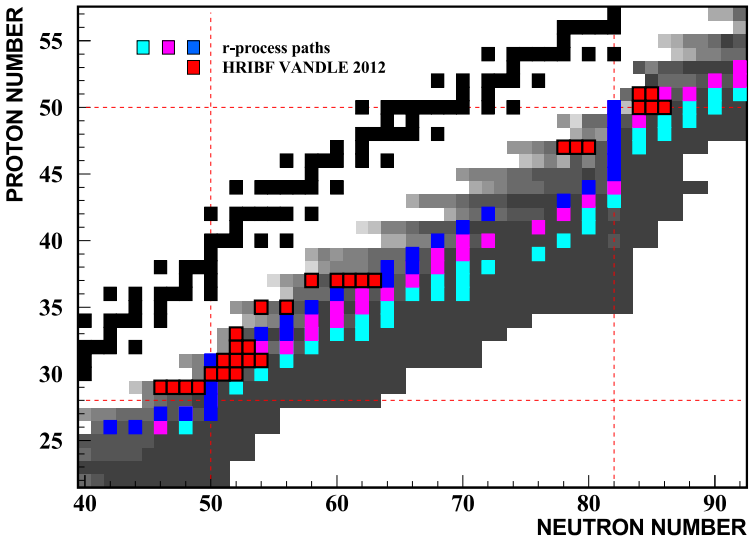


Figure 6.1: A summary of the VANDLE experiment performed in February 2012. Nuclei measured with VANDLE are in red boxes. The teal, pink, and blue boxes represent various r-process paths and the dashed lines represent the shell closures. Progressing shades of grey represent increasing $Q_{\beta-n}$ windows.

states from the $p_{3/2}$, $f_{5/2}$, $p_{1/2}$, and $g_{9/2}$ orbitals, see Figure 1.3, into their respective spin-orbit partner proton orbitals. For $^{78}$Ni these transitions connect the $0^+$ ground state to $1^+$ excited states in $^{78}$Cu with particle-hole configurations. The literature [7, 80, 81] characterizes these configurations as core-polarized states (CPS), spin-flip states (SFS), and back spin-flip states (BSFS). One may calculate the matrix elements for these configurations, which leads to the single particle picture in Figure 6.2. Table 6.1 lists the initial and final states for the CPS, SFS, and BSFS transitions for p,f,g shell. For $^{78}$Ni the SFS state is energetically forbidden. This model is a starting point for the following discussions. This work presents just a selection of the studied nuclei: $^{77,78}$Cu and $^{84}$Ga.

One may modify the ESPSM using the Tamm-Dancoff approximation [82, 83, 84], which uses a repulsive residual interaction to calculate the beta decay strength distribution. Within this framework a Giant Gamow-Teller resonance (GTR) appears due to the coherent sum of the individual particle-hole excitations. This

Table 6.1: The initial and final states for CPS, SFS, and BSFS transitions in the p,f,g shell. For $^{78}$Ni the SFS transition is energetically forbidden.

| Transition Type | Initial State | Final State |
|---|---|---|
| CPS | $2p_{3/2}$ | $2p_{3/2}$ |
| | $1f_{5/2}$ | $1f_{5/2}$ |
| | $2p_{1/2}$ | $2p_{1/2}$ |
| | $2g_{9/2}$ | $2g_{9/2}$ |
| SFS | $2p_{3/2}$ | $2p_{1/2}$ |
| | $1g_{9/2}$ | $1g_{7/2}$ |
| BSFS | $2p_{1/2}$ | $2p_{3/2}$ |

model concentrates the strength distribution into individual transitions, which is a simplification of reality.

A more sophisticated model, QRPA [13, 14, 85], produces larger fragmentation of the strengths that still contain the GTR. However, the GTR lies outside of the beta decay window. This model predicts a group of states lower in energy, pygmy GTR, that are composed of CPS and BSFS states [26]. In this model, the "pygmy" GTR enters into the beta decay window as one crosses the N=50 shell closure, see Figure 2 in Reference [26]; this causes a sudden jump in the beta delayed neutron branching ratios. The branching ratios would tend toward 100% were it not for the competition of the first forbidden transitions with the GT transitions.

Previous measurements in the region by Kratz et al. [28] claimed that the peak structure in the beta-delayed neutron spectra correspond to the existence of individual transitions, which we attribute to the pygmy resonances. Recall that this structure is dismissed by Hardy et al. [30] as statistical fluctuations due to a high density of states populated in beta decay. The cQRPA calculations by Borzov that include the pygmy resonance produce good agreement between lifetimes and neutron branching ratios [21, 86]. This indicates that the pygmy resonances are required and that the resonance structures in the B(GT) are expected. This work observes these B(GT) structures experimentally.

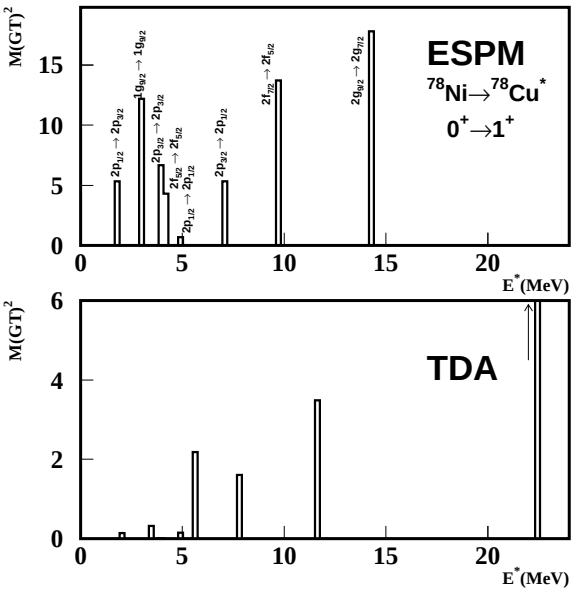


Figure 6.2: The decay of $^{78}$Ni into $^{78}$Cu using the extreme single particle model (top panel) and the Tamm-Dancoff Approximation. In both cases only the decays to $1^+$ states in the daughter nucleus are considered [1].

## 6.1 $^{77}$Cu

Armbruster et al. discovered $^{77}$Cu in 1987 using fission fragments from induced fission of $^{235}$U with the LOHENGRIN recoil separator [87]. Kratz et al. measured the half-life to be 469(8) ms [88]. The most comprehensive study of this nucleus comes from Ilyushkin et al. [67] where the $P_n$ was determined to be 30(20)%. This experiment used the ranging-out technique as well as LeRIBSS, and occurred at the HRIBF. The ranging-out technique provides an excellent method to determine the absolute branching ratios for the decays because the system counts the number of ions passing through it. In addition to the ranging-out, LeRIBSS provided a better determination of the half-life and allowed the gamma rays to be gated with beta detectors. Other groups studying $^{77}$Cu used similar methods to those described and more information may be found in References [89] and [69]. The ground state spin-parity of $^{77}$Cu is 5/2- as measured by Köster et al. [90] using in-source laser spectroscopy.

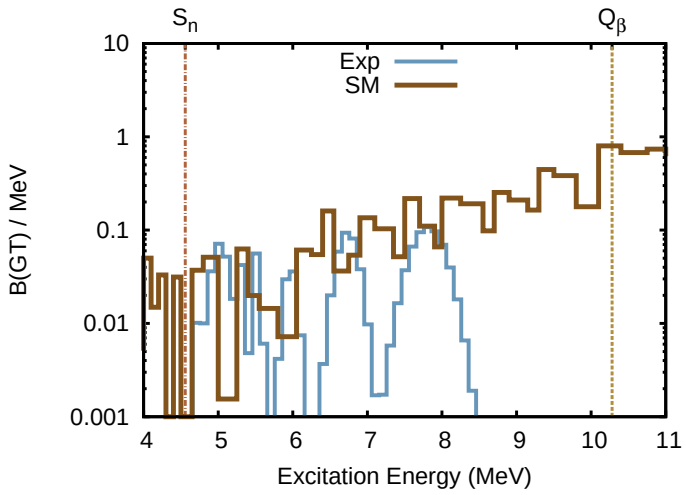


Figure 6.3: Experimental data (blue line) compared with calculations performed by Sieja et al. [2]. The vertical dashed line represents the neutron separation energy. For energies just above $S_n$ the B(GT) fluctuates rapidly due to Pandemonium. The experimental data show more distinct peak structure than the theoretical model.

Sieja et al. [2] performed shell model calculations for the strength distribution of $^{77}$Cu. These calculations included only GT transitions and predicted strengths for $3/2^-$, $5/2^-$, and $7/2^-$ states in $^{77}$Zn, and included all active orbitals in the f,p, and g shells. Figure 6.3 displays the results of this calculation as compared with the experimental B(GT). The strong fluctuations of the experimental B(GT) near the $S_n$ are due to Pandemonium, see Ch. 1. Interestingly, the experimental spectra show more distinct peak structure at higher energies than the calculations. The $Q_\beta$ value for the decay does not allow for determination of the B(GT) for higher energies. The comparisons between observed and modeled neutron spectra reinforce the discrepancy between observation and theory, see Figure 6.4. Here we use the statistical Hauser-Feshbach codes by Kawano et al. [32], which takes into account the centrifugal barrier that affects neutron emission and gamma-neutron emission competition. The neutron spectra from these calculations show less structure than the experimental spectra deduced from VANDLE.

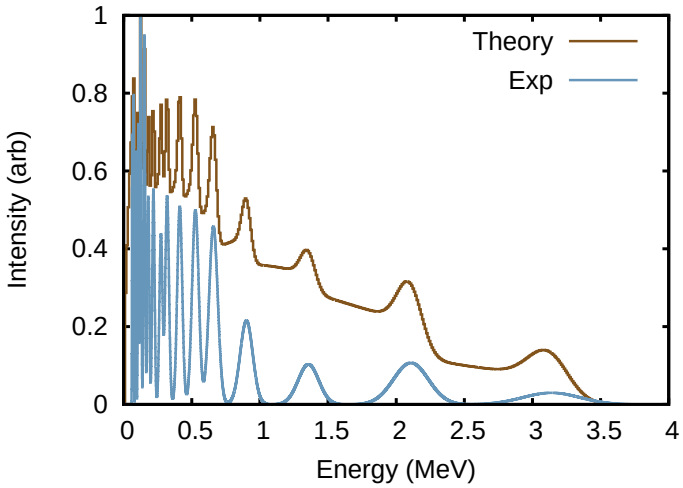


Figure 6.4: Experimental data for $^{77}$Cu (blue line) compared with calculations (brown line) performed by M. Bertolli using statistical codes by T. Kawano et al and the experimental B(GT) as input. We observe a large discrepancy between the experimental and theoretical neutron spectra.

## 6.2 $^{78}$Cu

Lund et al. discovered $^{78}$Cu in 1987 at Studsvik using the isotope separator on-line facility OSIRIS [91]. Pieffier et al. provides the first measurement of the $P_n$ to be $15^{+10}_{-5}$% [92], but the unknown energy of $\beta$ particles and unknown number of collected ions made the branching ratio unreliable. Subsequent work by van Roosbroeck at ISOLDE places a lower limit on the $P_n$ $\geq$65(20)% [93], which is in good agreement with Ref. [86]. A conflicting $P_n$ measured by Hosmer et al. [94] is lower than the previous measurements at 44.0(5.4)%. It was postulated that the discrepancy may be due to a previously unknown isomeric state in the daughter nucleus; however, this was ruled out by Köster et al. [90] who observed no isomeric states in the decay daughter. Finally, Korgul et al. measured the neutron branching ratio at the HRIBF using a combination of an MCP and an ion chamber together with high purity Ge clovers to precisely determine the number of implanted ions [69]. Their measurement of the branching ratio closely agrees with Refs. [93] and [86] and is 65(8)%.

The large B(GT) value for the $^{78}$Cu decay may be interpreted in the following way. the large $Q_\beta$ value for this decay (13.0 MeV) along with the high neutron branching ratio (65(8)%) provides the possibility of seeing a larger portion of the GT pygmy resonance states located within the $Q_\beta$ window.

## 6.3 $^{84}$Ga

Kratz et al. discovered $^{84}$Ga in 1991 [88] using induced fission of a $^{238}$UC target and identified it using the ISOLDE on-line mass separator. Since its discovery, several groups studied the decay using high resolution gamma ray detectors [95, 96, 97]; however, few gammas have been associated with the decay due to the large neutron branching ratio. Of importance to this work, Kratz et al. measured the $P_n$ to be 70(15)% [88]. Winger et al. studied the nucleus at the HRIBF and provides a measured neutron branching ratio of 74(14)% [18], which is consistent with previous measurements. The most recent measurement by Kolos et al. expanded the known level schemes for $^{83,84}$Ge [98].

The decay of $^{84}$Ga has a $Q_\beta$ window of 13.9 MeV. This nucleus is past the N=50 shell closure, which means that particle-hole excitations are 3 MeV higher in energy than for N<50 nuclei, according to mass measurements by Hakala et al. [99]. This nucleus displays the most prominent peak structure for high energy neutrons that can be attributed to the GT pygmy resonance postulated by Borzov [26]. Figure 6.5 shows the comparison between the predictions by Borzov and the cQRPA and the experimental spectra. The figure demonstrates the while the VANDLE data reveals evidence for the pygmy resonance, there is a discrepancy between the strength distributions.

In addition, we have performed statistical model calculations using the experimental B(GT) spectra, Figure 6.6. Because the ground state spin-parity of $^{84}$Ga is unknown, we postulated spins and parities for the g.s. to range between $0^-$ to $5^-$. These calculations indicate a preference for a $5^-$ g.s. of $^{84}$Ga. Here the centrifugal

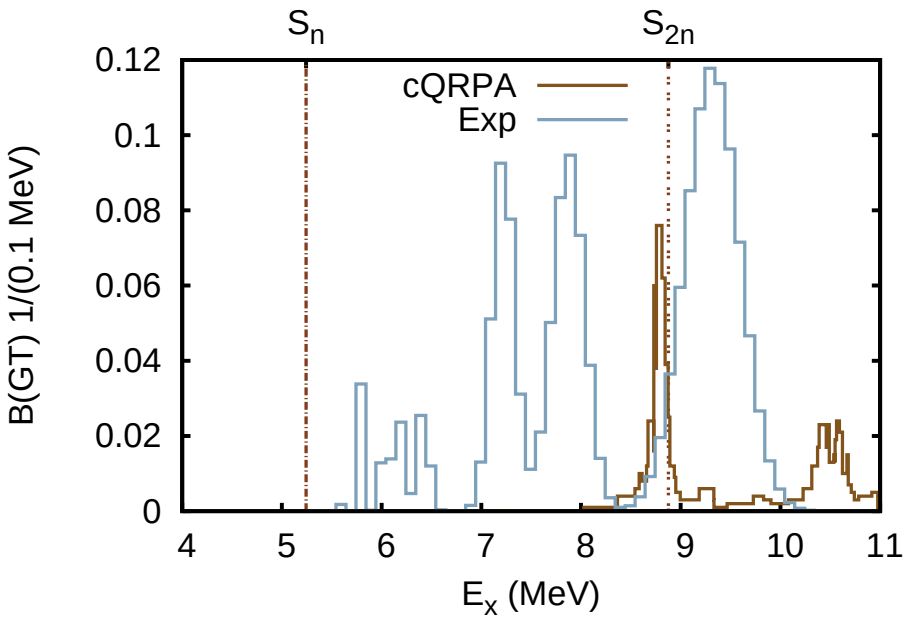


Figure 6.5: A comparison between the experimental B(GT) (blue) and cQRPA calculations by Borzov. Both spectra show evidence for the pygmy resonance, but differ on the energy at which it occurs.

barrier, combined with the relatively low density of high spin states, prevents the emission of low energy neutrons to excited states in $^{83}$Ge. A similar situation is likely to occur for $^{78}$Cu, where the spin-parity of the g.s. is postulated at $5^-$.

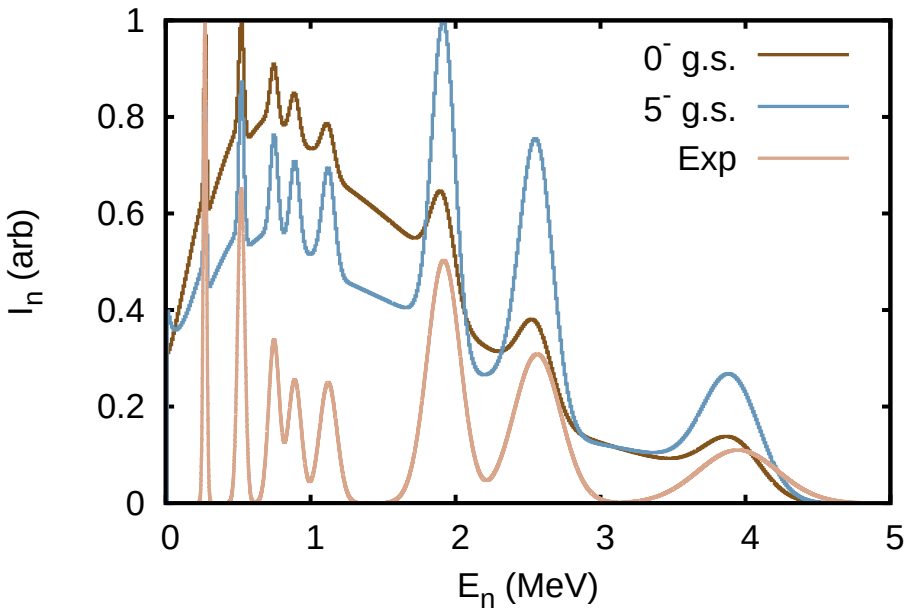


Figure 6.6: A comparison between the experimental intensity and the statistical model calculations using the experimental B(GT) as input. The ratio of high energy to low energy neutrons (cutoff 1.5 MeV) indicates a preference for the $5^-$ g.s. over the $0^-$. Calculations are performed by M. Bertolli using the statistical codes written by Kawano et al.

# Chapter 7

# Summary

This work sought to measure the beta-delayed neutron energies from fission fragments. This was the first such attempt since the 1990s and the first to investigate cases with a large energy window available for neutron emission. The neutron spectra and what they tell us about the nuclear structure has important impact on theoretical models, the astrophysical r-process, and on nuclear reactor design.

A central part of this work was the development and implementation of the Versatile Array of Neutron Detectors at Low Energy. VANDLE uses the time-of-flight technique to deduce neutron energies. A digital data acquisition system instruments the entire array. To ensure that the digital system met the timing requirements necessary for time-of-flight measurements, we investigated three timing algorithms. Of the three algorithms only one, the fitting algorithm, had the necessary resolution over the full dynamic range. A new method for validation of timing methods applied to digitized signals provided a quick and efficient method to ensure that the timing algorithms produce accurate results, and can be used to benchmark other digital timing algorithms in the figure. This part of the work is currently in the review process for publication in Nuclear Instruments and Methods A [100].

Upon completion of VANDLE, we performed an experimental campaign at the Holifield Radioactive Ion Beam Facility, measuring the beta-delayed neutron spectra

for nearly thirty fission fragments in the $^{78}$Ni and $^{132}$Sn regions for the first time. The experiment used purified radioactive ion beams delivered to LeRIBSS and measured the decay products using a combination of beta detectors, VANDLE and germanium detectors. To analyze the data from VANDLE, we developed a complete software framework, VAST, which reconstructs the strength distributions from the measured time-of-flight spectra. The neutron spectra for the most prominent cases have been analyzed and the beta strength distribution presented.

The case of $^{77}$Cu demonstrates the need for gamma coincidences to unfold the proper strength distribution since the gamma gated ToF spectra appear similar to the ungated spectra. This indicates that a significant portion of the neutron distribution originates from states of higher excitation energy than it appears from the singles spectrum. The remaining cases, $^{78}$Cu and $^{84}$Ga display unexpected, prominent high energy peak structures in their neutron spectra, the latter being exceptionally pronounced. It is postulated that these strong resonances are due to the pygmy GT resonances that appear in QRPA calculations. These strong fluctuations appear not to be due to Pandemonium effects, and we have implemented a procedure of using statistical models of the deexcitation of states populated in beta decay to check the consistency of the extraction of the Gamow-Teller strength from neutron spectra. We have made a first attempt to compare our results with theoretical predictions. The novelty of our data will hopefully inspire more theoretical work on prediction of Gamow-Teller strength distributions.

# Bibliography

[1] Żylicz, J., Dobaczewski, J. & Szymanski, Z. Gamow-Teller decay of even isotopes $^{68}$Ni to $^{78}$Ni. *AIP Conf. Proc.* **455**, 813–815 (1998). URL http://link.aip.org/link/?APC/455/813/1. xv, 62, 65

[2] Sieja, K. & Nowacki, F. Shell quenching in $^{78}$Ni: A hint from the structure of neutron-rich copper isotopes. *Phys. Rev. C* **81**, 061303 (2010). URL http://link.aps.org/doi/10.1103/PhysRevC.81.061303. xvi, 66

[3] Gamow, G. & Teller, E. Selection Rules for the $\beta$-Disintegration. *Phys. Rev.* **49**, 895–899 (1936). URL http://link.aps.org/doi/10.1103/PhysRev.49.895. 1

[4] Konopinski, E. J. & Uhlenbeck, G. E. On the Fermi Theory of $\beta$-Radioactivity. *Phys. Rev.* **48**, 7–12 (1935). 1

[5] Konopinski, E. J. & Uhlenbeck, G. E. On the Fermi Theory of $\beta$-Radioactivity. II. The "Forbidden" Spectra. *Phys. Rev.* **60**, 308–320 (1941). URL http://link.aps.org/doi/10.1103/PhysRev.60.308. 1

[6] Krane, K. S. *Introductory Nuclear Physics* (John Wiley & Sons, Inc., 1988). 3

[7] Grotz, K. & Klapdor, H. *The Weak Interaction in Nuclear, Particle, and Astrophysics* (IOP Publishing, 1990). 3, 61, 63

[8] Mayer, M. G. Nuclear Configurations in the Spin-Orbit Coupling Model. I. Empirical Evidence. *Phys. Rev.* **78**, 16–21 (1950). URL http://link.aps.org/doi/10.1103/PhysRev.78.16. 3

[9] Mayer, M. G. Nuclear Configurations in the Spin-Orbit Coupling Model. II. Theoretical Considerations. *Phys. Rev.* **78**, 22–23 (1950). URL http://link.aps.org/doi/10.1103/PhysRev.78.22. 3

[10] Caurier, E., Martínez-Pinedo, G., Nowacki, F., Poves, A. & Zucker, A. P. The shell model as a unified view of nuclear structure. *Rev. Mod. Phys.* **77**, 427–488 (2005). 4

[11] Lanczos, C. An iteration method for the solution of the eigenvalue problem of linear differential and integral operators. *Journal of Research of the National Bureau of Standards* **45**, 255–282 (1950). 4

[12] Möller, P. & Randrup, J. New developments in the calculation of $\beta$-strength functions. *Nuclear Physics A* **514**, 1–48 (1990). URL http://www.sciencedirect.com/science/article/pii/037594749090330O. 4

[13] Borzov, I. N., Fayans, S. A., Krömer, E. & Zawischa, D. Ground state properties and $\beta$-decay half-lives near $^{132}$Sn in a self-consistent theory. *Z. Phys. A* **355**, 117–127 (1996). 4, 64

[14] Möller, P., Pfeiffer, B. & Kratz, K. L. New calculations of gross $\beta$-decay properties for astrophysical applications: Speeding-up the classical r process. *Phys. Rev. C* **67** (2003). 4, 64

[15] Takahashi, K. & Yamada, M. Gross Theory of Nuclear $\beta$-Decay. *Progress of Theoretical Physics* **41** (1969). 4

[16] Lisetskiy, A. F., Brown, B. A. & Horoi, M. Exotic nuclei near $^{78}$Ni in a shell model approach. *Eur. Phys. J. A* **25**, 95–96 (2005). 5

[17] Ilyushkin, S. V. *et al.* $\beta$-decay studies of the transitional nucleus $^{75}$Cu and the structure of $^{75}$Zn. *Phys. Rev. C* **83**, 014322 (2011). 5

[18] Winger, J. *et al.* New subshell closure at N=58 emerging in neutron-rich nuclei beyond $^{78}$Ni. *Phys. Rev. C* **81**, 044303 (2010). 5, 68

[19] Burbidge, E. M., Burbidge, G. R., Fowler, W. A. & Hoyle, F. Synthesis of the Elements in Stars. *Rev. Mod. Phys.* **29**, 547 (1957). 5

[20] Nishimura, S. *et al.* $\beta$-Decay Half-Lives of Very Neutron-Rich Kr to Tc Isotopes on the Boundary of the r-Process Path: An Indication of Fast r-Matter Flow. *Phys. Rev. Lett.* **106**, 052502 (2011). 5

[21] Madurga, M. *et al.* New Half-lives of r-process Zn and Ga Isotopes Measured with Electromagnetic Separation. *Phys. Rev. Lett.* **109**, 112501 (2012). 5, 64

[22] Yoshida, T. & Nichols, A. L. (eds.) *Assessment of Fission Product Decay Data for Decay Heat Calculations*, vol. 25 of *Nuclear science, NEA 6284* (OECD Nuclear Energy Agency, 2007). By the Working Party on International Evaluation Co-operation of the NEA Nuclear Science Committee ; co-ordinator, T. Yoshida, monitor, A.L. Nichols. 5

[23] McMillan, E. Radioactive Recoils from Uranium Activated by Neutrons. *Phys. Rev.* **55**, 510 (1939). 6

[24] Winger, J. A. *et al.* Test of the singly magic character of the N = 50 isotone $^{83}$As populated in $^{83}$Ge decay. *Phys. Rev. C* **38** (1988). 7

[25] Padgett, S. *et al.* $\beta$ decay of $^{81}$Zn and migrations of states observed near the N=50 closed shell. *Phys. Rev. C* **82**, 064314 (2010). 7

[26] Borzov, I. N. $\beta$-delayed neutron emission in the $^{78}$Ni region. *Phys. Rev. C* **71**, 065801 (2005). 7, 8, 64, 68

[27] Rudstam, G., Shalev, S. & Jonsson, O. Delayed neutron emission from separated fission products. *NIM* **120**, 333 – 344 (1974). URL

http://www.sciencedirect.com/science/article/pii/0029554X7490055X. 8, 62

[28] Kratz, K. L. *et al.* Investigation of Beta strength functions by neutron and gamma-ray spectroscopy. *Nucl. Phys. A* **317**, 335–362 (1979). 8, 62, 64

[29] Hardy, J., Carraz, L., Jonson, B. & Hansen, P. The essential decay of pandemonium: A demonstration of errors in complex beta-decay schemes. *Physics Letters B* **71**, 307 – 310 (1977). URL http://www.sciencedirect.com/science/article/pii/0370269377902234. 8

[30] Hardy, J. C., Jonson, B. & Hansen, P. G. The essential decay of pandemonium: $\beta$-delayed neutrons. *Nucl. Phys. A* **305**, 15–28 (1978). 8, 64

[31] Hauser, W. & Feshbach, H. The Inelastic Scattering of Neutrons. *Phys. Rev.* **87**, 366–373 (1952). URL http://link.aps.org/doi/10.1103/PhysRev.87.366. 8

[32] Kawano, T., Möller, P. & Wilson, W. B. Calculation of delayed-neutron energy spectra in a quasiparticle random-phase approximation-Hauser-Feshbach model. *Phys. Rev. C* **78**, 054601 (2008). 8, 66

[33] Matei, C. *et al.* The Versatile Array of Neutron Detectors at Low Energy (VANDLE). In *Proceedings of The Ninth International Symposium on Nuclei in the Cosmos*, vol. 138, 1–5 (Proceedings of Science, 2008). 11

[34] Peters, W. A. *et al.* Performance of the Versatile Array of Neutron Detectors at Low Energy (VANDLE). *In Preparation* (2014). 11, 38

[35] Mitra, S., Wielopolski, L. & Hendrey, G. Comparison of a digital and an analog signal processing system for neutron inelastic gamma-ray spectrometry. *Appl. Radiat. Isot.* **61**, 1463 – 1468 (2004). URL

http://www.sciencedirect.com/science/article/pii/S0969804304001514. 11

[36] Al-Adili, A., Hambsch, F.-J., Oberstedt, S., Pomp, S. & Zeynalov, S. Comparison of digital and analogue data acquisition systems for nuclear spectroscopy. *NIMA* **624**, 684 – 690 (2010). URL http://www.sciencedirect.com/science/article/pii/S0168900210021595. 11

[37] Nyquist, H. Certain Topics in Telegraph Transmission Theory. *Transactions of the American Institute of Electrical Engineers* **47**, 617–644 (1928). 11, 13

[38] Fallu-Labruyere, A., Tan, H., Henning, W. & Warburton, W. K. Time resolution studies using digital constant fraction discrimination. *NIMA* **579**, 247–251 (2007). 12, 16

[39] Blaich, T. *et al.* A large area detector for high-energy neutrons. *NIMA* **314**, 136 – 154 (1992). 12, 25

[40] Buţă, A. *et al.* TONNERRE: an array for delayed-neutron decay spectroscopy. *NIMA* **455**, 412–423 (2000). 12, 25

[41] Luther, B. *et al.* MoNA - The Modular Neutron Array. *NIMA* **505**, 33–35 (2003). 12, 25

[42] Perdikakis, G. *et al.* LENDA: A low energy neutron detector array for experiments with radioactive beams in inverse kinematics. *NIMA* **686**, 117 – 124 (2012). URL http://www.sciencedirect.com/science/article/pii/S0168900212005906. 12, 25, 40

[43] Aykac, M., Hong, I. & Cho, S. Timing performance comparison of digital methods in positron emission tomography. *NIMA* **623**, 1070–1081 (2010). 12

[44] Streun, M. *et al.* Coincidence detection by digital processing of free-running sampled pulses. *NIMA* **487**, 530–534 (2002). 12

[45] Bardelli, L., Poggi, G., Bini, M., Pasquali, G. & Taccetti, N. Time measurements by means of digital sampling techniques: a study case of 100 ps FWHM time resolution with a 100 MSample/s, 12 bit digitizer. *NIMA* **521**, 480–492 (2004). 12, 16

[46] Tektronix. *Arbitrary Function Generators : AFG3000C Series.* URL http://www.tek.com/signal-generator/afg3000-function-generator. 14

[47] Madurga, M. *et al.* Digital Electronics For The Versatile Array Of Neutron Detectors At Low Energies. *AIP Conf. Proc.* **1336**, 586–589 (2011). URL http://link.aip.org/link/?APC/1336/586/1. 15, 21

[48] Akima, H. A New Method of Interpolation and Smooth Curve Fitting Based on Local Procedures. *Journal of the Association for Computing Machinery* **17**, 589–602 (1970). 16

[49] Galassi, M. *et al. GNU Scientific Library Reference Manual* (Network Theory Ltd., 2009). URL https://www.gnu.org/software/gsl/manual/html_node/. Accessed on line; 10 January 2013. 16, 17

[50] Matei, C. *et al.* Development of a Versatile Array of Neutron Detectors at Low Energy. *AIP Conf. Proc.* **1099**, 790–793 (2009). URL http://link.aip.org/link/?APC/1099/790/1. 25

[51] Zecher, P. *et al.* A large-area, position-sensitive neutron detector with neutron/$\gamma$-ray discrimination capabilities. *NIMA* **401**, 329–344 (1997). URL http://www.sciencedirect.com/science/article/pii/S016890029700942X. 25

[52] Knoll, G. F. *Radiation Detection and Measurement* (John Wiley & Sons, Inc., 2000). 27, 28, 46

[53] Birks, J. B. *Scintillation Counters*. Pergamon Science Series (McGraw-HMcGraw-Hill Book Co., Inc., 1953), 1 edn. 27

[54] Birks, J. B. The Specific Fluorescence of Anthracene and Other Organic Materials. *Phys. Rev.* **84**, 364–365 (1951). URL http://link.aps.org/doi/10.1103/PhysRev.84.364.2. 27

[55] Birks, J. B. Theory of the Response of Organic Scintillation Crystals to Short-Range Particles. *Phys. Rev.* **86**, 569–569 (1952). URL http://link.aps.org/doi/10.1103/PhysRev.86.569. 27

[56] Madey, R., Waterman, F. M., Baldwin, A. R. & Knudson, J. N. The Response of NE-228A, NE-228, NE-224, and NE-102 Scintillators to Protons from 2.43 to 19.55 MeV. *NIM* **151**, 445–450 (1978). 28

[57] Flyckt, S.-O. & Marmonier, C. (eds.) *Photomultiplier Tubes : Principles and Applications* (Photonis Imaging Sensors, 2002). 30

[58] Starosta, K. *et al.* Digital Data Acquisition System for experiments with segmented detectors at National Superconducting Cyclotron Laboratory. *NIMA* **610**, 700–709 (2009). URL http://www.sciencedirect.com/science/article/pii/S0168900209017392. 38, 39

[59] Massey, T. N. *et al.* A Measurement of the $^{27}$Al($d$,$n$) Spectrum for Use in Neutron Detector Calibration. *Nucl. Sci. Eng.* **129**, 175–179 (1998). 39

[60] Manhart, W. Status of the Cf-252 fission-neutron spectrum evaluation with regard to recent experiments. *Proceedings of the Consultants Meeting on Physics of Neutron Emission in Fission, Mito City, Japan* **Report INDC(NDS)-220**, 305–336 (1988). 40

[61] Agostinelli, S. *et al.* Geant4 - a simulation toolkit. *NIMA* **506**, 250 – 303 (2003). URL

http://www.sciencedirect.com/science/article/pii/S0168900203013688. 40

[62] Beene, J. R. *et al.* Radioactive Ion Beam Production Capabilities At The Holifield Radioactive Ion Beam Facility. *AIP Conf. Proc.* **1336**, 576–580 (2011). URL http://link.aip.org/link/?APC/1336/576/1. 43

[63] Kofoed-Hansen, O. & Kristensen, P. Short-Lived Krypton Isotopes and Their Daughter Substances. *Phys. Rev.* **82**, 96–96 (1951). URL http://link.aps.org/doi/10.1103/PhysRev.82.96. 43

[64] Stracener, D. *et al.* Targets used in the production of radioactive ion beams at the HRIBF. *NIMA* **521**, 126 – 135 (2004). URL http://www.sciencedirect.com/science/article/pii/S0168900203030742. ¡ce:title¿Accelerator Target Technology for the 21st Century. Proceedings of the 21st World Conference of the International Nuclear Target Society¡/ce:title¿. 43

[65] *What is HRIBF*. On line (2005). URL http://www.phy.ornl.gov/hribf/misc/whatishribf.shtml. Accessed 02 January 2013. 43, 44

[66] Rykaczewski, K. *Low-energy Radioactive Ion Beam Spectroscopy Station (LeRIBSS)*. On line (2008). URL http://www.phy.ornl.gov/hribf/equipment/leribss/. Accessed 10 October 2013. 44

[67] Ilyushkin, S. V. *et al.* $\beta$ decay of the $\pi f_{5/2}$ ground state of $^{77}$Cu studied with 225 MeV and 0.2 MeV purified radioactive beams. *Phys. Rev. C* **80** (2009). 46, 52, 65

[68] Debertin, K. & Helmer, R. G. *Gamma- and X-Ray Spectrometry With Semiconductor Detectors* (North-Holland Publishing Company, 1988). 46

[69] Korgul, A. *et al.* $\beta$-$\gamma$ and $\beta$-delayed neutron-$\gamma$ decay of neutron-rich copper isotopes. *Phys. Rev. C* **86**, 024307 (2012). 52, 65, 67

[70] Bevington, P. R. & Robinson, K. D. *Data Reduction and Error Analysis for the Physical Sciences* (McGraw-Hill, 2003). 55

[71] Myung, I. J. Tutorial on maximum likelihood estimation. *J. Math. Psychol.* **47**, 90–100 (2003). 56

[72] Oreglia, M. J. *A Study of the Reactions* $\psi' \to \gamma\gamma\psi$. Ph.D. thesis, Stanford University (1980). 56

[73] Gaiser, J. E. *Charmonium Spectroscopy from Radiative Decays of the* $J/\psi$ *and* $\psi'*$. Ph.D. thesis, Stanford University (1982). 56

[74] Skwarnicki, T. *A Study of the Radiative Cascade Transitions Between the Upsilon-Prime and Upsilon Resonances.* Ph.D. thesis, Cracow Institute of Nuclear Physics (1986). 56

[75] Verkerke, W. & Kirkby, D. *RooFit Users Manual v2.91*, 2.91-33 edn. (2008). 57

[76] Brun, R. & Rademakers, F. {ROOT} - An object oriented data analysis framework. *NIMA* **389**, 81 – 86 (1997). URL http://www.sciencedirect.com/science/article/pii/S016890029700048X. 57

[77] James, F. & Roos, M. Minuit - a system for function minimization and analysis of the parameter errors and correlations. *Computer Physics Communications* **10**, 343–367 (1975). URL http://www.sciencedirect.com/science/article/pii/0010465575900399. 57

[78] Greenwood, R. C. & Watts, K. D. Delayed Neutron Energy Spectra of $^{87}$Br, $^{88}$Br, $^{89}$Br, $^{90}$Br, $^{137}$I, $^{138}$I, $^{139}$I,$^{136}$Te. *Nucl. Sci. Eng.* **126**, 324–332 (1997). 62

[79] Yee, R. M. *et al.* $\beta$-Delayed Neutron Spectroscopy Using Trapped Radioactive Ions. *Phys. Rev. Lett.* **110**, 092501 (2013). URL http://link.aps.org/doi/10.1103/PhysRevLett.110.092501. 62

[80] Bergdolt, G., Bergdolt, A., Klapdor, H. & Schrader, M. The M1 strength distribution in the $\gamma$-decay of the $g_{9/2}$ analogue state in $^{61}$Cu. *Nucl. Phys. A* **263**, 477 – 490 (1976). URL http://www.sciencedirect.com/science/article/pii/0375947476902013. 63

[81] Jänecke, J. *et al.* Fragmentation of Gamow-Teller strength observed in $^{117,120}$Sn($^{3}$He, $t$ )$^{117,120}$Sb charge-exchange reactions. *Phys. Rev. C* **48**, 2828–2839 (1993). URL http://link.aps.org/doi/10.1103/PhysRevC.48.2828. 63

[82] Dancoff, S. M. On Radiative Corrections for Electron Scattering. *Phys. Rev.* **55**, 959–963 (1939). 63

[83] Mandelstam, L. & Tamm, I. The Uncertainty Relation Between Energy And Time In Non-Relativistic Quantum Mechanics. *Journal of Physics (USSR)* **9**, 249–254 (1945). 63

[84] Dancoff, S. M. Non-Adiabatic Meson Theory of Nuclear Forces. *Phys. Rev.* **78**, 382–385 (1950). 63

[85] Borzov, I. N. Gamow-Teller and first-forbidden decays near the r-process paths at N = 50,82, and 126. *Phys. Rev. C* **67**, 025802 (2003). 64

[86] Winger, J. A. *et al.* Large $\beta$-delayed neutron emission probabilities in the $^{78}$Ni Region. *Phys. Rev. Lett.* **102**, 142502 (2009). 64, 67

[87] Armbruster, P. *et al.* Identification of the New Neutron-Rich Isotopes $^{70-74}$Ni and $^{74-77}$Cu in Thermal Neutron Fission of $^{235}$U. *Europhys. Lett.* **4**, 793 (1987). URL http://stacks.iop.org/0295-5075/4/i=7/a=006. 65

[88] Kratz, K.-L. *et al.* Neutron-rich isotopes around the r-process "waiting-point" nuclei $^{29}_{79}$Cu$_{50}$ and $^{30}_{80}$Zn$_{50}$. *Z. Phys. A* **340**, 419–420 (1991). URL http://dx.doi.org/10.1007/BF01290331. 65, 68

[89] Patronis, N. *et al.* $\beta$-decay study of $^{77}$Cu. *Phys. Rev. C* **80**, 034307 (2009). 65

[90] Köster, U. *et al.* In-source laser spectroscopy of $^{75,77,78}$Cu: Direct evidence for a change in the quasiparticle energy sequence in $^{75,77}$Cu and an absence of longer-lived isomers in $^{78}$Cu. *Physical Review C* **84**, 034320 (2011). 65, 67

[91] Lund, E., Ekstrom, B., Fogelberg, B. & Rudstam, G. Identification and half-life determination of very neutron-rich copper isotopes. *AIP Conf. Proc.* **164**, 578–580 (1987). URL http://link.aip.org/link/?APC/164/578/1. 67

[92] Pfeiffer, B., Kratz, K. L. & Möller, P. Status of delayed-neutron precursor data: half-lives and neutron emission probabilities. *Progress in Nuclear Energy* **41**, 39–69 (2002). 67

[93] Van Roosbroeck, J. *et al.* Evolution of the nuclear structure approaching $^{78}$Ni:$\beta$ decay of $^{74-78}$Cu. *Phys. Rev. C* **71**, 054307 (2005). URL http://link.aps.org/doi/10.1103/PhysRevC.71.054307. 67

[94] Hosmer, P. *et al.* Half-lives branchings for $\beta$-delayed neutron emission for neutron-rich Co-Cu isotopes in the r-process. *Phys. Rev. C* **82**, 025806 (2010). 67

[95] Perru, O. *et al.* Decay of neutron-rich Ga isotopes near N = 50 at PARRNe. *Phys. At. Nucl.* **66**, 1421–1427 (2003). URL http://dx.doi.org/10.1134/1.1601744. 68

[96] Lebois, M. *et al.* Experimental study of $^{84}$Ga $\beta$ decay: Evidence for a rapid onset of collectivity in the vicinity of $^{78}$Ni. *Phys. Rev. C* **80**, 044308 (2009). URL http://link.aps.org/doi/10.1103/PhysRevC.80.044308. 68

[97] VERNEY, D. *et al.* STRUCTURE OF THE NEUTRON RICH Ga AND Ge ISOTOPES OBSERVED AT ALTO. *International Journal of Modern Physics E* **18**, 1976–1980 (2009). URL http://www.worldscientific.com/doi/abs/10.1142/S0218301309014111. http://www.worldscientific.com/doi/pdf/10.1142/S0218301309014111. 68

[98] Kolos, K. *et al.* Probing nuclear structures in the vicinity of $^{78}$Ni with $\beta$- and $\beta$n-decay spectroscopy of $^{84}$Ga. *Phys. Rev. C* **88**, 047301 (2013). URL http://link.aps.org/doi/10.1103/PhysRevC.88.047301. 68

[99] Hakala, J. *et al.* Evolution of the $N = 50$ Shell Gap Energy towards $^{78}$Ni. *Phys. Rev. Lett.* **101**, 052502 (2008). URL http://link.aps.org/doi/10.1103/PhysRevLett.101.052502. 68

[100] Paulauskas, S. V. *et al.* A Digital Data Acquisition Framework for the Versatile Array of Neutron Detectors at Low Energy. *NIMA* **Accepted** (2013). 71

# Vita

Stay a while and listen. The author was born in the cold snow strewn plains of Kansas on February 2 in the year of Our Lord 1985 imparting an affinity for burrowing woodland creatures. He moved to the more temperate state of Tennessee in the year of Our Lord 1992. The author attended Fred J. Page High School in Rudderville, unincorporated, where his junior year physics class awoke a passion deep within his loins. He then resolved to dedicate his life to his new found love. He graduated high school in the year of Our Lord 2003.

Having his fill of the Nashville Basin, the author climbed eastward to the Highland Rim to begin his studies at Tennessee Technological University. The author had the opportunity to teach physics labs associated with the general physics classes, and found that being a mentor to students was a rich and fulfilling experience. These positions allowed the author to explore various applications in physics, and participate in experiments at the HRIBF at ORNL. These experiences cemented a passion for nuclear physics, which continues to this very day. The author received his Bachelor's of Science Degree in Physics in the year of Our Lord 2007.

The author completed his slow march out of the Nashville Basin, crossed the Cumberland Plateau, and settled in the Tennessee River Valley to attend the University of Tennessee at Knoxville, where he completed his Doctor of Philosophy Degree in Nuclear Physics in December in the year of Our Lord 2013 and then embarked on a quest for pure knowledge and enjoyment.